

Global Gravity Wave Variances from Aura MLS: Characteristics and Interpretation

Dong L. Wu¹ and Stephen D. Eckermann²

¹ Jet Propulsion Laboratory, California Institute of Technology, Pasadena, California.

² Space Science Division, Naval Research Laboratory, Washington DC.

Last updated: September 17, 2007

Submitted to: J. Atmos. Sci. (the special issue on Imbalance)

Corresponding author:

Dong Wu

M/S 183-701

Jet Propulsion Laboratory, California Institute of Technology

4800 Oak Grove Drive, Pasadena, California 91109

Phone: 818-393-1954

Fax: 818-393-5065

Email: Dong.L.Wu@jpl.nasa.gov

Abstract

The gravity wave (GW) resolving capabilities of 118 GHz saturated thermal radiances acquired throughout the stratosphere by the Microwave Limb Sounder (MLS) on the Aura satellite are investigated and initial results presented. Since the saturated (optically-thick) radiances resolve GW perturbations from a given altitude at different horizontal locations, we evaluate variances at 12 pressure altitudes between ~ 21 and 51 km using the 40 saturated radiances found at the bottom of each limb scan. Forward modeling simulations show that these variances are controlled mostly by GWs with vertical wavelengths $\lambda_z > 5$ km and horizontal along-track wavelengths of $\lambda_y \sim 100$ -200 km. The tilted cigar-shaped three-dimensional weighting functions yield highly selective responses to GWs of high intrinsic frequency that propagate towards the instrument. We use the latter property to infer the net meridional component of GW propagation by differencing the variances acquired from ascending (A) and descending (D) orbits. Due to its improved vertical resolution and sensitivity, Aura MLS GW variances are ~ 5 -8 times larger than those from UARS MLS. Like UARS MLS variances, monthly mean Aura MLS variances in January and July, 2005 are enhanced when local background wind speeds are large, due to GW visibility effects. Zonal asymmetries in variance maps reveal enhanced GW activity at high latitudes due to forcing by flow over major mountain ranges, and at tropical and subtropical latitudes due to enhanced deep convective generation as inferred from contemporaneous MLS cloud-ice data. At 21-28 km altitude (heights not measured by UARS MLS), GW variance in the tropics is systematically enhanced and shows clear variations with the phase of quasi-biennial oscillation, in general

agreement with GW temperature variances derived from radiosonde, rocketsonde and limb-scan vertical profiles. GW-induced temperature variances at ~ 44 km altitude derived from operational global analysis fields of the European Centre for Medium-Range Weather Forecasts Integrated Forecast System in August 2006 reveal latitudinal bands of enhanced GW variance and preferred GW meridional propagation directions that are similar to those inferred from the MLS variances, highlighting the potential of MLS GW data for validating the stratospheric GWs simulated and/or parameterized in global models.

1 Introduction

Gravity waves (GWs) play a key role in the global meteorology, climate, chemistry and microphysics of the stratosphere and mesosphere (Fritts and Alexander, 2003). Since finite computational resources force global climate-chemistry and weather prediction models to run at spatial resolutions that do not adequately resolve GW dynamics, these important GW-induced effects must be parameterized (e.g., McLandress, 1998; Kim et al., 2003). Arguably the greatest weakness in current GW parameterizations is their poorly constrained specifications of lower atmospheric sources (see, e.g., McLandress and Scinocca, 2005). While it is recognized that GWs can be excited by flow across mountains, convection, and imbalance/instability within rapidly evolving baroclinic jet/frontal systems (e.g., Fritts et al., 2006), the relative contributions of these sources to the GW spectrum encountered in the middle atmosphere remains highly uncertain, particularly with respect to GWs radiated from jet imbalance (see, e.g., section 7h of Kim et al., 2003).

Direct measurements of GWs by advanced satellite remote sensors can reduce some of these uncertainties (Wu et al. 2006a). One of the first satellite instruments to provide global measurements of stratospheric GWs was the Microwave Limb Sounder (MLS) on the Upper Atmosphere Research Satellite (UARS) (Wu and Waters, 1996, 1997). Those measurements provided initial insights into some of the major orographic and deep convective sources of GWs for the middle atmosphere (e.g., McLandress et al., 2000; Jiang et al., 2002, 2004a, 2004b, 2005, 2006). A new MLS instrument on the Earth Observing System (EOS) Aura satellite started acquiring data in July, 2004. In this study we extend the analysis of GWs using saturated thermal

stratospheric radiances from the UARS MLS to the new radiances now being acquired by Aura MLS. The new instrument was designed to measure atmospheric composition with emphasis on the upper troposphere and lower stratosphere (UT/LS). One of the seven Aura MLS radiometers measures thermal O₂ emission features near 118 GHz with sensitivity, vertical resolution and spectral coverage that are all much improved over UARS MLS 63 GHz measurements acquired during 1991-1997. Thus, the Aura MLS 118 GHz radiances are more sensitive to GWs than earlier UARS MLS 63 GHz measurements.

The stratospheric GWs observed by MLS differ from those observed by other satellite instruments in at least two important ways. First, the MLS GW product is not derived from the retrieved temperature, as with other limb sounders such as LIMS (Limb Infrared Monitor of the Stratosphere) (Fetzer and Gille, 1994), CRISTA (Cryogenic Infrared Spectrometers and Telescopes for the Atmosphere) (Preusse et al., 2002), GPS/MET occultation (Tsuda et al., 2000), and SABER (Sounding of the Atmosphere using Broadband Emission Radiometry) (Preusse et al., 2006). These techniques deduce atmospheric pressure/temperature from optically-thin radiances and can measure GW-induced temperature perturbations with slightly better vertical resolution but relatively poorer horizontal resolution than MLS. Thus, the resolved GW-induced temperature variances from these instruments correspond to different portions of the three-dimensional (3-D) GW wavenumber spectrum than those based on saturated radiances (Wu et al., 2006a). Second, the MLS radiance responses to GW-induced temperature perturbations are very sensitive to the wave's horizontal propagation direction, unlike GW data from nadir sounders, such as AMSU-A (Advanced Microwave Sounding Unit-A) (Wu, 2004) and AIRS (Atmospheric Infrared Sounder) (Alexander and Barnett, 2007), and from other limb sounders,

such as LIMS, CRISTA and SABER. Because MLS has a very shallow viewing angle (3° - 8° above the local horizon) and a narrow field-of-view (FOV), its saturated radiances have 3-D weighting functions (WFs) that are tilted up from the horizon with an aspect ratio of $\sim 1:10$ for the vertical-to-horizontal length scales. When tilted GW phase structures coalign with these tilted WFs, they produce a strong radiance perturbation signal. As a result, the GW-induced radiance variance observed by MLS can differ significantly, depending on the viewing direction with respect to horizontal GW propagation. Thus, variance differences for the same GWs observed by MLS from different viewing angles can be used to infer anisotropies in GW horizontal propagation directions (Jiang and Wu, 2001). Such a viewing-dependent difference in response is clearly evident after sorting monthly-mean variances from ascending (i.e., satellite latitude increasing with time) and descending (i.e., satellite latitude decreasing with time) orbits (Wu and Waters, 1997).

The paper is organized as follows. Section 2 describes the Aura MLS instrument, focusing on the 118GHz thermal channels that resolve GW perturbations in saturated radiance measurements. Section 3 outlines our variance calculations, and the sensitivity of these radiance variances to GWs of different wavelengths and horizontal propagation directions. Section 4 presents these variances as a function of altitude, season, and geographical location to infer information on stratospheric GW amplitudes, horizontal propagation directions and source characteristics. In section 5, MLS GW variances are cross-correlated at 45 km altitude in August, 2006 with small-scale GW-induced temperature oscillations explicitly resolved in high-resolution global analysis fields issued by the ECMWF (European Centre for Medium-Range Weather Forecasts) IFS (Integrated Forecast System). Section 6 summarizes major results from this study and briefly

discusses areas for future work.

2 The MLS Experiment on Aura

Aura MLS scans the atmospheric limb continuously. Each scan, also called a major frame (MAF), takes 24.7s, covers tangent heights h_t ranging from the surface ($h_t \sim 0$) to ~ 92 km (Waters et al., 2006), and is separated horizontally from adjacent scans by ~ 165 km. Each MAF is further divided into 148 minor frames (MIFs) with ~ 120 MIFs devoted to atmospheric measurements.

We focus here on thermal radiances from the 25 channels centered on the strong 118 GHz O_2 line (channel 13) and its various wing line emissions that are distributed symmetrically about the center line and that saturate at progressively lower heights in the atmosphere (see Table 1). In the normal operation mode (Waters et al., 2006), each of these Aura MLS channels yields more than 40 saturated radiance measurements at the bottom of each scan which can be used for GW analysis, compared to only 6 saturated measurements in the UARS MLS 63 GHz thermal radiance channels. According to radiative transfer theory, the saturated microwave radiance is a direct measurement of blackbody emission of atmospheric air at a particular altitude layer defined by the temperature WF. Fluctuations in the saturated radiances occur due to air temperature fluctuations within that layer, and one can derive GW-induced temperature variance from these radiance fluctuations. The increased number of saturated radiance measurements from Aura MLS means that the GW variance can be estimated more precisely using data from a single scan.

Because GWs have 3-D phase structures that depend on phase speed, propagation direction and the background environment, the MLS viewing geometry, which affects the orientation and

shape of the WFs, is important for understanding its sensitivity to various types of GWs. The Aura MLS 118 GHz radiance channels have an angular FOV with full-width half maximum (FWHM) of $\sim 0.113^\circ$, corresponding to a vertical width of ~ 4.9 km (Cofield and Stek, 2006) at the volume where the radiance is saturated, which is located ~ 2500 km from the spacecraft. The UARS MLS 63 GHz FOV is $\sim 0.206^\circ$, or ~ 9.6 km vertical width at the limb (Jarnot et al., 1996; Wu and Waters, 1996), much broader than that of the Aura MLS. Another important difference for GW detection is that UARS MLS observed at 90° to the spacecraft motion, whereas Aura MLS observes along the direction of spacecraft motion. The Aura MLS cross-track FOV at 118 GHz is $\sim 0.23^\circ$ (Cofield and Stek, 2006), or ~ 10 km at the limb. Because of the forward viewing Aura MLS geometry, this cross-track width of the 3-D WF has a much smaller influence on GW detection compared to much longer WF widths along-track. Therefore, in this paper we focus only on how the two-dimensional (2-D) WF cross-sections along the orbit plane affect GW detection. Unlike UARS, Aura does not make periodic yaw maneuvers that interrupt sampling patterns, and so the forward-viewing Aura MLS measurements cover latitudes between 82°S and 82°N every day.

Aura MLS can resolve GW perturbations down to UT/LS altitudes using radiances from other frequency channels located well away from the 118GHz O_2 line. Because most GWs are generated in the troposphere, these new UT/LS GW observations are especially valuable in pushing the MLS GW measurements down closer to source regions. MLS GW observations in the troposphere rely primarily on the four wideband channels at 115.2, 117.0, 120.5, and 122.0 GHz. However, the 115.2 and 122.0 GHz radiances can be contaminated by cloud scattering while the 117.0 and 120.5 GHz channels have fewer than 40 useful saturated radiance

measurements. Since MLS GW variances are sensitive to the number of radiance measurements used in the calculation (see, e.g., Fig. 3 of Jiang et al., 2002), here we require that each channel must have 40 saturated radiance measurements in a given scan, which limits our study to the 25 channels near 118 GHz and excludes the wideband measurements. As shown in Fig.1a (see also Table 1), the lowest temperature WF peak from these 25 channels occurs at a pressure height of ~ 21.7 km.

Fig.1b shows these various channel radiances from an MLS scan located near the northern tip of the Antarctic Peninsula at 04:02:48 UTC on 2 September 2004. Large-amplitude oscillations are evident in the saturated portions of the radiance profiles measured at low h_i ; the thick solid line in Fig. 1b roughly demarks the unsaturated upper-level radiances from the saturated lower-level radiances for each channel. When a limb radiance saturates, the altitude of its temperature WF (see Fig.1a) remains roughly constant even though the instrument is scanning vertically. In this case, as depicted in Fig. 2a, vertical scanning then leads to *horizontal* displacement of the atmospheric volumes yielding the saturated limb radiances. We fit, then remove, a linear trend (due to a slight change in viewing angle) in the saturated radiances to isolate perturbations. The perturbations in saturated radiances from a given channel arise due to horizontal temperature variations at the channel's saturation altitude (see Fig. 2a). Fig. 1c plots the perturbations extracted from the saturated radiances from channels 1-12 in Fig. 1b, mapped (based on the saturation altitude and viewing tangent height) to the precise latitude and longitude of the volume along the line-of-sight (LOS) ray to the altitude where the channel is saturated (Fig. 1a): the variation of MLS LOS with latitude is shown in Fig. 2b. This remapping procedure yields in Fig. 1c variations as a function of latitude (and longitude, not shown) at each channel's saturation

pressure altitude, which ranges from ~ 22 km for channels 1 and 25 to ~ 51 km for channels 12 and 14 (see Table 1), assuming a constant scale height of 6.95 km. The along-track distances spanned by the saturated limb radiances in a given MAF vary between 1° and 4° (or 100-400 km) during normal operation (see Fig. 1c), which is determined by the satellite motion (~ 7 km s^{-1}), the MLS scan rate, and the number of saturated radiance measurements in each channel (see Fig. 1b). For the GW event isolated in Fig. 1c, the wave-induced radiance amplitude exceeds 10 K in channels 10-12, has an along-track wavelength of ~ 200 km, and shows linear phase tilting with altitude, the “fingerprint” of a gravity wave oscillation.

To compute GW-induced variances, we use the 40 saturated radiances observed by a single channel at the bottom of each scan during normal operation (Fig. 1b) and estimate the radiance variance for this channel in this scan. Thus, each MLS GW variance is uniquely associated with a radiance channel, which in turn is identified with a characteristic pressure altitude, defined here as the peak of the vertical WF for that channel’s saturated radiances (Fig. 1a). The GW variance derived from these data is fundamentally different from variances deduced from the retrieved temperature, for which the retrieval algorithm has combined unsaturated radiances from multiple channels in a least-squares sense to yield a temperature profile that varies vertically, not horizontally. In the radiance variance analysis used here, although some higher-altitude channels may contain more than 40 saturated radiances, it is important to apply a uniform truncation of 40 points to all channel data since the GW variances are very sensitive the truncation length used (e.g., McLandress et al., 2000; Jiang et al., 2002). The 40-pt cutoff corresponds to a horizontal truncation length of ~ 140 km along track, and therefore GWs with along-track horizontal wavelengths longer than this do not contribute significantly to these variances.

3 Variance and Sensitivity Analyses

a) GW Variance Calculation

The GW variance calculation is carried out as follows. The 40 saturated radiances are first fitted with a linear function. Then, the residuals from the fit are combined for the symmetric channel pairs (e.g, channels 1 and 25: see Table 1) since they have similar WFs and the signal-to-noise ratio of the resulting variance is improved by a factor of 2 compared to single channel variances. The resulting radiance variance (hereafter called the 40-pt variance) contains contributions from instrument noise (σ_e^2) and GW-induced variance (σ_{GW}^2), namely,

$$\sigma^2(n) = \sigma_{GW}^2(n) + \sigma_e^2(n) \quad , \quad (1)$$

where n denotes channel number from 1(25) to 12(14). As shown in Fig. 1c, each scan produces 12 GW variance estimates, each of which has a unique pressure altitude determined by that channel's WF peak.

We can derive the GW variance using Eq. (1) if the radiance variance and noise can both be estimated accurately: i.e. $\sigma_{GW}^2(n) = \sigma^2(n) - \sigma_e^2(n)$. For Aura MLS, the noise variance σ_e^2 can be determined with high precision using radiance measurements at high tangent heights where there is no atmospheric signal, However, as described by Wu and Waters (1997) for UARS MLS, the σ^2 estimate is subject to statistically-random noise that dominates the final uncertainty of the

σ_{GW}^2 estimate. Uncertainties in the measured variance $\hat{\sigma}^2$ depend on the noise variance σ_e^2 in the case where $\sigma_{GW}^2 \ll \sigma_e^2$. Wu and Waters (1997) showed that the estimated variance $\hat{\sigma}^2$ has an uncertainty of $\sqrt{2/(M-2)}\sigma_e^2$ for M -pt variance estimation, which yields $\sim 0.23\sigma_e^2$ for $M=40$, a value sometimes too large to permit statistically significant σ_{GW}^2 estimates. Thus, further averaging is required to reduce uncertainties in the final σ_{GW}^2 estimate.

One approach to improving the σ_{GW}^2 statistics is to average the variance measurements over a period of time or over a large geographical region. The variance uncertainty will be reduced to $0.23\sigma_e^2/\sqrt{J}$ if J is the number of independent variance measurements that are averaged. A tradeoff between spatial and temporal averaging needs to be made, depending on the GW problems of interest. Averaging over a long period of time helps to detect weak GW variances over an isolated geographical region (e.g., Jiang et al., 2004a) but removes information on short-term variability. On the other hand, variances averaged over a large geographical domain (e.g., zonal means) can yield statistically significant GW information on daily time scales, but with the loss of regional information (e.g., zonal asymmetries). If GWs occur persistently or frequently over a given geographical region, we typically choose to average the variances over a long period of time (say, one month) within a small region, such as a $5^\circ \times 10^\circ$ latitude-longitude box. Within a $5^\circ \times 10^\circ$ grid box, Aura MLS typically produces ~ 6 profiles every 5 days from just the ascending orbits alone, which would improve the minimum detectable variance of channel 1(25) to 5.6×10^{-3}

K^2 . For a monthly mean, this lower limit can be reduced still further to $2.3 \times 10^{-3} K^2$. Estimated noise variances σ_e^2 and statistical uncertainties for σ_{GW}^2 under various averaging scenarios are listed in Table 1 for all 12 MLS channel pairs. In section 4 we analyze GW variances σ_{GW}^2 derived from some of these different averaging scenarios.

In addition to the variance averaging, the truncation length M used in the variance calculation can also affect the value of minimum detectable GW variance. Since stratospheric GWs show larger temperature variances at long horizontal wavelengths (e.g., Bacmeister et al., 1996; Koshyk and Hamilton, 2001; Wu, 2001), a longer truncation length should yield larger GW variance values. In the MLS case, truncation length is limited by the number of saturated radiances within each scan, except for special limb-tracking operations where saturated data sequences can span thousands of kilometers. UARS MLS limb-tracking observations show that GW variances increase exponentially with horizontal scales between 100 and 1000 km (McLandress et al., 2000; Wu, 2001; Jiang et al., 2002).

b) MLS GW Visibility Function

As with other GW-resolving satellite sensors (Alexander, 1998; McLandress et al., 2000; Preusse et al., 2002; Jiang et al., 2004a; Wu, 2004; Eckermann and Wu, 2006), interpreting Aura MLS variances requires a comprehensive understanding of the instrument's sensitivity to GWs of different wavelengths and propagation directions. Specifying this so-called MLS GW visibility function in turn requires knowledge of the 3-D temperature WFs of the saturated limb radiance. As discussed in section 2, because Aura MLS scans within the orbital plane in the forward

direction, the most critical part of the WF for GW detection is the 2-D cross section in the along-track (along-scan) direction, also known as the orbital plane. Fig. 2a schematically depicts a series of these 2-D WF cross sections: as with UARS MLS, the width in the cross-scan direction is narrow and determined mainly by the $\sim 0.23^\circ$ horizontal FOV of the antenna. In the orbital plane, MLS WFs appear as narrow, cigar-shaped volumes that are tilted $\sim 3^\circ$ - 8° from the local horizon at their saturation altitude. As with saturated UARS MLS radiances, this tilting is a net effect of the MLS viewing angle, antenna spreading at the saturation altitude, and the width and shape of the vertical temperature WF (Wu and Waters, 1997; McLandress et al., 2000; Jiang et al., 2004a). The MLS sensitivity to GWs of short vertical wavelengths is determined primarily by the FOV's vertical FWHM, which is 4.9 km, even though the long dimension of the cigar-shaped WF can stretch to over 10 km vertically (see Fig. 2a). More accurate radiative transfer calculations show that the cigar-shaped volume approximates the 2-D WF cross section quite well, except near the bottom of the WFs where strong absorption breaks the symmetry about the LOS axis slightly and skews the WF shapes (Wu and Waters 1997).

We model the 2-D MLS GW visibility functions in the along-scan (y - z) plane by convolving the 2-D instrument WFs through an infinite plane temperature wave of 1 K amplitude and given values of vertical (λ_z) and along-track (λ_y) wavelength. The signs of λ_z and λ_y are chosen such that the GW energy propagates upwards and towards the instrument. Microwave absorption is approximated using a Lorentz-lineshape approximation (e.g., Eckermann and Wu, 2006) and peaks at a pressure height of ~ 30 km, roughly approximating saturated radiances from Channels 6(20). The resulting 2-D WFs are computed using realistic microwave radiative transfer, antenna spreading and spherical geometry (Cofield and Stek, 2006) on a 2-D grid of 100 m vertical and

1000 m horizontal resolution. From the simulated (forward-modeled) radiance perturbations, we compute the 40-pt radiance variances using the same method outlined in section 3a, and repeat the simulation for the full range of possible λ_y and λ_z wavelength pairs.

The calculated 2-D visibility function for MLS 40-pt variances is shown in Fig. 3a. The peak variance sensitivity occurs at $\lambda_y \sim 130$ km and $\lambda_z \sim 14$ km, where the variance calculated from the simulated radiances (brightness temperatures) is 0.47 K^2 , representing $\sim 94\%$ “visibility” to the input GW’s actual temperature variance of 0.5 K^2 . This is a case where the GW propagates upward and towards MLS and its phase lines, tilted off the horizontal at an angle $\phi = \tan^{-1}(\lambda_z/\lambda_y) \sim 6^\circ$, are nearly parallel to the instrument’s similarly tilted 2-D WF in Fig. 2a, so that there is essentially no smearing of wave phase along the LOS direction. When this same GW propagates away from the instrument (λ_y changes sign), the variance response becomes negligible ($< 6 \times 10^{-3} \text{ K}^2$) since phases are no longer coaligned with the 2-D WFs and appreciable LOS smearing occurs. This directional sensitivity is now studied further.

Fig.3a shows that Aura MLS sensitivity to along-track wavelengths tapers off at $\lambda_y < \sim 100$ km and $\lambda_y > \sim 170$ km. The diminishing sensitivity at short λ_y is due to the along-track smearing by the antenna pattern, satellite motion, and radiative transfer, whereas at long λ_y it is due to the 40-pt truncation. The smearing effects of radiative transfer and MLS FOV also limit the sensitivity to waves of small λ_z and $\lambda_y = 100\text{-}200$ km.

Fig.3b indicates that Aura MLS has optimal sensitivity to GWs with λ_z/λ_y aspect ratios of ~ 0.1 that yield a tilt angle ϕ similar to those of the 2-D WFs. From the hydrostatic non-rotating GW dispersion relation, this implies peak sensitivity to GWs with intrinsic frequencies $\omega = (\lambda_z/\lambda_y) N$

$\sim 0.1N$, where N is the background Brunt-Väisälä (BV) frequency, or intrinsic wave periods of ~ 1 hour given typical stratospheric BV periods of ~ 5 min. Thus these 40-pt variances are most sensitive to medium-scale GWs of relatively high intrinsic frequency. The variances have poor sensitivity to low-frequency inertia GWs, which, from the dispersion relation, have λ_z/λ_y ratios of ~ 0.01 - 0.001 . In other words, inertia GWs surviving MLS WF filtering will have long λ_y values that will not survive the 40 pt horizontal truncation.

c) Sensitivity to horizontal propagation

The highly directional tilting of the UARS MLS 2-D WFs yielded a complex 3-D in-orbit sensitivity to GWs that is depicted schematically in Fig. 2 of Jiang et al. (2004a) and was modeled in detail by McLandress et al. (2000) and Jiang et al. (2004a) to aid comparisons between model results and observations. As depicted in Fig. 2a, the 2-D tilted Aura MLS WFs will also yield a directional sensitivity in the response to GWs, though it is different from UARS MLS in terms of viewing direction, channel specifics and antenna widths.

The Aura satellite is in a 98.2° -inclination orbit, and the onboard MLS views the atmosphere directly ahead of the satellite (i.e., in the direction of the satellite velocity vector). This yields an MLS LOS (y) axis directed 8.2° from the meridional plane at latitudes near the equator (Fig. 2b). As we have noted in section 3b and Fig. 3, upward-propagating GWs with $\lambda_z > \sim 10\text{km}$ and $\lambda_z/\lambda_y \sim 0.1$ are well detected by MLS when they propagate towards the instrument, but yield little or no signal when propagating away from the instrument. As a result, at low latitudes, the GW variances from the ascending (A) and descending (D) orbits, $\sigma_A^2(n)$ and $\sigma_D^2(n)$, respectively, are

sensitive mostly to GWs propagating southward $\sigma_s^2(n)$ and northward $\sigma_N^2(n)$, respectively, but with a small eastward/westward component $\sigma_{EW}^2(n)$ in both cases. Mathematically, we may express this as

$$\sigma_A^2(n) = \sigma_s^2(n) + \sigma_{EW}^2(n), \quad (2a)$$

$$\sigma_D^2(n) = \sigma_N^2(n) + \sigma_{EW}^2(n), \quad (2b)$$

where n is channel number. In Eqs. (2a) and (2b) we assume that $\sigma_A^2(n)$ and $\sigma_D^2(n)$ are sufficiently averaged to be not biased by any transient large-amplitude GW event. Thus, $\sigma_A^2(n)$ and $\sigma_D^2(n)$ reflect the same ensemble mean GW variance with the same mean net eastward/westward propagation component, $\sigma_{EW}^2(n)$. With these assumptions, Eqs. (2a) and (2b) reveal that the ascending minus descending ($A-D$) variance, $\sigma_A^2(n) - \sigma_D^2(n)$, can be used to estimate the variance asymmetry between southward and northward propagating GW components, $\sigma_s^2(n) - \sigma_N^2(n)$. Thus, a positive A-D variance suggests dominance of GWs with a southward component to their wave propagation, relative to those with a northward component.

At mid- and high-latitudes, the $\sigma_{EW}^2(n)$ component in Eqs. (2a) and (2b) will become larger as the MLS LOS deviates further from the meridional plane (to $\sim 16.7^\circ$ at $\pm 60^\circ$ latitude; see Fig. 2b).

Nonetheless, as long as the mean GW ensemble sampled by the ascending and descending orbits is the same, the A - D variance remains a good proxy for the asymmetry in variance between GWs with southward and northward components to their horizontal phase propagation. Note that any systematic mean diurnal variation in GW variance is neglected in this interpretation of the A - D variance.

d) Sensitivity to short vertical wavelengths

High-resolution suborbital observations suggest that GW temperature variances in the stratosphere are dominated by GWs with vertical wavelengths between ~ 2 and 10 km (e.g., Tsuda et al., 1991; Allen and Vincent, 1995; Whiteway, 1999). Therefore, it is important to determine precisely the MLS sensitivity to GWs at these short vertical wavelengths. The visibility simulations in Fig. 3a reveal that 1K temperature perturbations induced by GWs of $\lambda_z=5$ km and $\lambda_y\sim 50$ -100 km can produce a radiance variance of ~ 0.02 K². Though weak, such a variance is certainly measurable by Aura MLS because of the low instrument noise. As indicated in Table 1, the MLS radiometric noise in channel 1(25) allows GW variance of $\geq 2.3 \times 10^{-3}$ K² to be detected in a $5^\circ \times 10^\circ$ monthly map, or in daily zonal averages with 5° latitude bins. Moreover, a 0.02 K² GW variance can even show out in a 5-day $5^\circ \times 10^\circ$ map for channel 1(25), where the estimated noise floor in Table 1 is $\sim 5.6 \times 10^{-3}$ K². GW observations at 5-day temporal resolution or better are often needed to monitor transient GW events like those reported by Wu and Zhang (2004) and Eckermann et al. (2006b).

These noise and visibility estimates confirm that the Aura MLS sensitivity to GWs at short vertical wavelengths is greatly improved over UARS MLS, due mainly to the narrower

beamwidth (i.e., vertical FOV) of the new instrument. In particular, for waves with $\lambda_z=5$ km, the Aura MLS vertical FOV of 0.113° provides 2 orders of magnitude greater sensitivity than UARS MLS.

4 Initial Results from Aura MLS

a) Zonal Mean Variances

Figs. 4-5 show zonal mean ascending and descending GW variances and the $A-D$ variance differences from Aura MLS for January and July 2005, respectively. Despite instrumental and viewing/sampling differences, the morphology of these Aura MLS GW variances is very similar to that of corresponding UARS MLS variances at altitudes above 30 km for 1992-1993 (Wu and Waters, 1996). Increased zonal-mean GW variances in Figs. 4a and 5a correlate very well with corresponding increases in the zonal-mean zonal wind speeds in the stratosphere, showing large variances at winter high latitudes within the summer and winter stratospheric jets. These correlations follow from the hydrostatic non-rotating GW dispersion relation, in which the vertical wavelength refracts in the presence of background winds and temperatures as

$$\lambda_z = \frac{2\pi|c - U \cos\phi|}{N}, \quad (3)$$

where c is ground-based horizontal phase speed, U is background wind speed, N is background BV frequency, and ϕ is the difference between the wind vector and GW horizontal propagation

directions. Extratropical stratospheric wind jet speeds $|U|$ are large and increase with height, which cause some GWs refract to critical levels ($\lambda_z \rightarrow 0$) where they are removed, and others to refract via Eq. (3) to long vertical wavelengths and propagate rapidly through the stratosphere. This can have two potential effects on the variance observed by MLS. First, the waves refracted to long λ_z become much more visible to MLS, while those refracted toward critical levels soon become invisible (see Fig. 3). Second, a high background wind can allow more waves with low phase speeds c to propagate through the stratosphere because they will not encounter stratospheric critical levels. For example, most of orographic GWs are generated with low phase speeds c , and therefore more wave energy is likely to propagate upwards in regions where background winds are strong. Both effects can enhance measured variances and must be carefully separated.

For example, UARS MLS GW variances exhibited strong correlations with background wind speeds due to the far greater overall visibility of the GW spectrum to MLS in regions with fast background winds (Alexander 1998). These strong effects had to be carefully accounted for in order to isolate additional signals in the variances from wave sources such as mountains and convection (e.g., McLandress et al. 2000; Jiang et al., 2004a). On the other hand, GW variances from satellite instruments with higher vertical resolution suffer less from this effect by resolving a wider range of vertical wavelengths (e.g., Tsuda et al. 2000; Preusse et al., 2006). Of particular interest here is to assess how the much improved vertical resolution of Aura MLS impacts direct detection of geophysical GW variance signals compared to UARS MLS.

In Figs. 4-5 the MLS GW variances show a general increase with height at all latitudes. One

important exception is in the tropical and subtropical lower stratosphere, where variances are larger than those values immediately above and poleward. Equatorially-confined enhancements in lower stratospheric GW temperature variance like these have been observed previously in high vertical resolution satellite limb data (e.g., Fetzer and Gille, 1994; Preusse et al., 2000; Tsuda et al., 2000, 2004; Ratnam et al., 2004) and suborbital profile data (Eckermann et al., 1995; Allen and Vincent, 1995). This tropical enhancement is not present in UARS MLS variances (see, e.g., Fig. 12 of Wu and Waters, 1997) because the instrument did not have an enough frequency bandwidth to observe below 28 km altitude where this feature appears most strongly. Work by Preusse et al. (2000) suggested that the coarse UARS MLS vertical WFs could not resolve this equatorial enhancement even if its channels extended to these lower altitudes. Thus, its occurrence in Aura MLS variances provides a clear demonstration of the much improved sensitivity of this new MLS instrument to short GW vertical wavelengths, as described in section 3d.

Nonetheless, we do not see a latitudinally symmetric equatorial variance enhancement in the lower stratosphere. The variances in January 2005 exhibit slight double peaks at $\pm 20^\circ$ latitudes where the background wind speeds have local maxima, while the relatively lower equatorial variance is associated with a weak eastward background wind and a deep convection peak as indicated by MLS cloud ice observations (Wu et al., 2006b), which are plotted as the dashed curves in Figs. 4-5. In July 2005, the subtropical enhancement at 21-25 km is confined to northern latitudes, which correlates well with enhanced wind speeds and deep convection at these latitudes, a feature previously reported in UARS MLS variances by Jiang et al. (2004b).

Two main theories for the equatorial enhancement in lower stratospheric GW variance have

been proposed. Eckermann (1995) interpreted the observed feature in rocket data as equatorial trapping of short- λ_z Kelvin modes. Alexander et al. (2002) attributed it to enhanced variances in short- λ_z low-frequency GWs that are supported at tropical latitudes by the decrease in inertial frequency that expands the range of allowed GW propagating frequencies. Interestingly, both theories interpret the enhanced variance as resulting from more waves with long horizontal wavelengths and low intrinsic frequencies near the equator, which these 40-pt MLS variances are largely insensitive to (see section 3b). The fact that an equatorial peak arises in these shorter-scale higher-frequency MLS GW variances too suggests that this feature observed by MLS may reflect a more general tropical enhancement in lower-stratospheric GW variances at all wavelength scales, possibly due to enhanced GW generation correlated with tropical tropospheric cloud ice (dotted curves in Figs. 4-5) and associated deep convection.

To infer meridional wave propagation anisotropies, zonal-mean A - D variances are plotted in Figs. 4c and 5c for January and July 2005, respectively. Assuming upward GW group propagation, the white lines superimposed on the statistically-significant positive and negative A - D values (see Table 1) depict the GW phase structures that are implied. In January 2005 (Fig. 4c), GWs near 40°N-60°N show preference for a northward component of propagation ($\sigma_A^2(n) - \sigma_D^2(n) < 0$) into the core of the strong upper stratospheric polar jet. This result is consistent with the conclusion inferred from UARS MLS limb-tracking GW variances in northern high-latitude winter by Jiang and Wu (2001), who found a strong cross-jet propagating GW component near the vortex edge. However, due to aliasing associated with UARS MLS sampling, their study could not identify absolute GW propagation directions. The Aura MLS $\sigma_A^2(n) - \sigma_D^2(n)$

maps confirm the presence of cross-jet propagating GWs near the vortex edge and suggest that waves here propagate preferentially northward on average. At 10°S-40°S and 10°N-20°N equatorward propagation components are preferred, while at latitudes south of 60°S, although the GW variances are weak, there is an overall tendency towards net southward propagation.

Similar poleward propagation tendencies at high latitudes are revealed in July 2005 (Fig. 5c). However, in the northern subtropics the inferred meridional propagation anisotropies are somewhat different to those in the southern subtropics for the opposite season (January 2005). Below 40 km southward propagation components are preferred, but above 40 km we infer dominant southward propagation at 60°S-40°S and 30°N-40°N and net northward propagation components at 10°N-20°N and 50°N-70°N.

Although UARS MLS and Aura MLS observe similar zonal mean climatologies of GW variance, the Aura MLS variances are 5-8 times larger than the UARS MLS values in the middle stratosphere, due partly to the greater sensitivity of Aura MLS to GWs with 2-10 km vertical wavelengths that dominate GW-induced stratospheric temperature variability. UARS MLS variances are also found to be weaker (by a factor of ~10) than AMSU-A variances at similar altitudes (Wu, 2004) due to different horizontal truncations used in the variance computations.

b) Monthly Maps

Figs. 6-7 plot monthly-mean global maps of $\sigma_A^2(n)$, $\sigma_D^2(n)$ and $\sigma_A^2(n) - \sigma_D^2(n)$ for different channels n that saturate at altitudes ranging from the lower to the upper stratosphere. Like the zonal means in Figs. 4a and 4b, the $\sigma_A^2(n)$ and $\sigma_D^2(n)$ maps in January 2005 (Fig. 6) show

significant enhancements at latitudes of the winter polar and the summer subtropical stratospheric jets. As discussed in section 4a, these latitudinal enhancements can be explained by the effects of wave refraction by the background wind, in which GWs attaining long vertical wavelengths in these high-wind regions become more visible to MLS. However, Fig. 6 shows that these enhancements are zonally asymmetric, which, as with similar features in UARS MLS maps, reveal the significant modulation of wave visibility by zonal asymmetries in stratospheric wind speeds as well as underlying wave sources (McLandress et al., 2000). Along the vortex edge, for instance, localized variance enhancements are closely tied to significant underlying topography in Alaska, Canada, southern Greenland, Scandinavia, and the Alps, suggesting these are due to large-amplitude orographic gravity waves. Detailed data analysis and global modeling by Jiang et al. (2004a) identified these and other Northern Hemisphere mountain ranges as sources of enhanced UARS MLS stratospheric radiance variance.

Although the zonal-mean $\sigma_A^2(n) - \sigma_D^2(n)$ in Fig. 4c suggested mean poleward propagation at 40°-60°N, the corresponding map in Fig. 6 reveals substantial zonal variability. While GWs over Alaska, the east coast of the United States (U.S.), southern Scandinavia and the Alps have preferred northward propagation components ($\sigma_A^2(n) - \sigma_D^2(n) < 0$), variance peaks over the Rockies and southern Greenland are dominated by waves with southward components to their propagation ($\sigma_A^2(n) - \sigma_D^2(n) > 0$).

In the subtropics, the $\sigma_A^2(n)$ and $\sigma_D^2(n)$ enhancements correlate very well with the MLS cloud ice distribution (white contours in Fig. 6), suggesting deep tropospheric convection over major

land masses and the maritime continent as the primary source of these regional variance increases. Similar features and correlations to tropical convection were noted in UARS MLS variances by McLandress et al. (2000) and Jiang et al. (2004b, 2005). As pointed out by Jiang et al. (2004b), the enhanced variances in the upper stratosphere are shifted slightly southeastward from the convective centers as waves propagate upwards from the forcing region. The filtering and refraction of GWs by the subtropical stratospheric jet can explain most of this shifted distribution since the jet core tilts away from the equator with altitude. However, it remains puzzling that the A - D maps in Fig. 6 suggest that these waves have preferred northward propagation components ($\sigma_A^2(n) - \sigma_D^2(n) < 0$) rather than southward propagation components in these regions.

Like the zonal means in Fig. 5a, global maps for July 2005 in Fig. 7 again show variances in the upper stratosphere that are enhanced at latitudes where background wind speeds are large, specifically along the winter polar stratospheric jet and over subtropical monsoons. The vortex enhancements show a non-uniform distribution in longitude with the highest variances near the southern tip of South America and the Antarctic Peninsula, a feature associated with large-amplitude orographic GWs that have been observed in these regions by a number of other satellite instruments (Eckermann and Preusse, 1999; McLandress et al., 2000; Tsuda et al., 2000; Preusse et al., 2002; Jiang and Wu, 2001; Jiang et al., 2002; Alexander and Teitelbaum, 2007). Enhanced variance due to orographic GWs is also observed over New Zealand, as was seen in UARS MLS radiance variances (Jiang et al. 2005). Broader vortex enhancements are also seen in regions well away from significant mountains, which may result in part from GWs radiated from imbalance within baroclinic jet/front systems at these latitudes (e.g., Guest et al. 2000; see section 5). The

corresponding A-D variance maps in Fig. 7 suggest a net poleward propagation tendency ($\sigma_A^2(n) - \sigma_D^2(n) > 0$) in this southern high-latitude band, consistent with the zonal means in Fig. 5c.

The pockets of enhanced variances in the northern subtropics seem to be mostly associated with American and Indian monsoon systems, as they again correlate well with similar enhancements in MLS cloud ice (white contours in Fig. 7). There is little latitudinal shift between the variance peak and deep convection in the Indian monsoon. However, the latitudinal shift over the American monsoon is significant, showing the variance peak displaced to the northeast from the deep convection center, and the displacement increases with height. Yet the *A-D* difference maps in Fig. 7 suggest that these GWs over the southeastern U.S. preferentially propagate to the south, rather than northward from convection centers. High-resolution radiosonde data also show a lower stratospheric GW variance enhancement over the southeastern US (Wang et al., 2003), with a preference for northward-eastward propagation in June-August (Wang, 2003). However, Wang et al. (2005) also inferred long horizontal wavelengths ($> \sim 500$ km) and low intrinsic frequencies for these GWs. The GWs resolved in the MLS variances have much shorter horizontal wavelengths and higher intrinsic frequencies, and thus may have fundamentally different sources and propagation characteristics. Thus the MLS GW activity in this region merits further investigation. For example, a similar feature is also seen in the Pacific just east of Japan in Fig. 7. Climatologically both regions experience typhoon/hurricane passages, which may generate some of this net southward-propagating stratospheric GW variance observed by MLS (e.g., Sato 1993; Kim et al., 2005)

The bottom panels of Fig. 6 show that the ascending variance at 21.7 km altitude in January

2005 has lower values in the equatorial band relative to the descending variance, and peaks in two subtropical bands (see also Fig. 4a), similar to tropical GW activity seen in GPS/CHAMP data during May 2001-January 2003 (Ratnam et al., 2004). The resulting subtropical A - D variances at 21.7 km in Fig. 6 are positive in the north and negative in the south (see also Fig. 4c), suggesting that the net meridional component of propagation of subtropical GWs observable by MLS in the lower stratosphere in January 2005 is equatorward in both hemispheres. However, the situation is quite different in January 2006 when the descending variances at 21.7 km exceed the ascending variances almost everywhere in the tropics (see also Fig. 8), implying widespread northward propagation components, and thus possible GW-QBO (Quasi Biennial Oscillation) interactions here (e.g., Eckermann et al., 1995; Vincent and Alexander, 2000; Wang and Geller, 2003). We investigate this further in section 4c. Over Indonesia and northern Australia, where GWs are presumably generated by active convective systems in the region (Tsuda et al., 2004), the A - D variances at 21.7 km in Fig. 6 suggest preferred northward propagation. Using a 3-D mesoscale cloud resolving model with realistic heating and background meteorological inputs, Alexander et al. (2004) found that convectively-generated GWs near Darwin, Australia were dominated by north-eastward propagation in November 2001. Their finding is consistent with the MLS climatology in November (see Fig. 8), which also exhibits negative A - D variances at 21.7 km in the Darwin region.

In July 2005, the subtropical A - D variances at 21.7 km altitude in Fig. 7 also show preferences for equatorward propagation components. The equatorial variance peaks at 21.7 km are displaced northward (see also Fig. 5a) because seasonal convective sources are mostly located on the summer side of the tropics. At higher altitudes, these subtropical peaks move further to the north

consistent with similar northward displacement with height of the core of the subtropical jet. The July 2006 variance maps in Fig. 8 exhibit a similar morphology.

c) Seasonal Variations

Fig. 8 plots monthly-mean variances at 21.7 km for each month of 2006. Due to QBO modulation, the tropical variances are larger in early 2006 when the QBO is in the easterly (westward) phase. In January 2006, GW variance maximizes near the equator with slight longitudinal variations, with secondary high-latitude peaks occurring over Greenland and Europe. As the QBO changes to the westerly phase, the tropical variance starts to split into two latitudinal bands after June 2006. By August-October the equatorial variances have weakened substantially and variance maps are dominated by enhancements over southern South America, Antarctica and the Southern Ocean.

Fig. 9 shows a time series of monthly zonal mean $\sigma_A^2(n)$, $\sigma_D^2(n)$, and their difference as a function of latitude at selected altitudes. The major annual and vertical variations are controlled by seasonally-varying background winds, which filter some GWs and refract others via Eq. (3) to long (short) vertical wavelengths that are more (less) visible to the instrument (Alexander, 1998). Although MLS GW variances are dominated by these annual variations, there is also a clear correlation between the QBO and MLS GW variances in the tropical lower stratosphere, most noticeably in Fig. 9 at 27.3 km altitude (~ 20 hPa), where the amplitude of the zonal-wind QBO peaks (Baldwin et al., 2001). At 21.7 km altitude, the tropical GW variance in Fig. 9 exhibits a latitudinal distribution with double peaks in 2004-2005 during a westerly QBO phase but a broad equatorially-centered peak in 2005-2006 during an easterly QBO phase. The $A-D$ variances at

15°S-15°N show net equatorward propagation during the W→E (westerly-to-easterly) QBO transition, and net poleward propagation during the E→W transition.

The equatorial GW variances at 21.7, 24.3 and 27.1 km in Fig. 9 all peak when the easterly phase of the QBO reaches its maximum. Rocketsonde, radiosonde, and satellite limb temperatures also find equatorial GW variances peaking during periods of strong QBO easterlies and that, immediately above in descending westerly QBO shear zones, wave variances are suppressed (Eckermann et al., 1995; Sato and Dunkerton, 1997; Vincent and Alexander, 2000; Randel and Wu, 2005; Wu, 2006; de la Torre et al., 2006; Krebsbach and Preusse, 2007).

Fig. 9 also reveals variance enhancements at 21-25 km altitude at 70°-80°S that occur around October-November of each year. These enhancements are particularly interesting because they do not correlate with corresponding increases in the zonal-mean zonal winds, like GW enhancements at other latitudes, heights and times. Inspection of raw maps at these times (Fig. 8) reveals variance enhancements at pressure altitudes below 30 km over a broad area of the Antarctic continent as the vortex shifts off the pole during the vortex breakup season. Large increases in GW temperature variance at ~20 km altitude over Antarctica during late spring have previously been reported using radiosonde data (Pfenniger et al. 1999; Yoshiki and Sato, 2000; Yoshiki et al. 2004) and GPS/CHAMP occultation data (Baumgaertner and McDonald, 2007). Above 20-25 km, the peak GW variances in these studies tend to occur in mid-winter (Yoshiki and Sato, 2000; Baumgaertner and McDonald, 2007), also in agreement with the MLS GW variances in Fig. 9.

In the middle and upper stratosphere the latitude-season trends of GW variances (e.g., at 44.1 km in Fig. 9) are very similar to those seen in UARS MLS variances (Wu and Waters, 1997),

showing a dominant annual variation at latitudes poleward of 30° . In the tropics, the QBO modulation seen lower down weakens and gives way to weaker modulation by the tropical stratospheric semiannual oscillation (SAO) in the upper stratosphere, in agreement with equatorial GW temperature variances from suborbital data (e.g., Eckermann et al. 1995). The extratropical wave variances are generally larger in the southern hemisphere (SH) than those in the northern hemisphere (NH) for both ascending and descending measurements, which may be a visibility effect due to generally stronger stratospheric wind jets in the SH.

Fig. 9 shows considerable differences in high-latitude variance between different northern winters, consistent with the well-known interannual variability of the entire Arctic winter stratosphere. Qualitatively similar interannual variability in high-latitude UARS MLS GW variance was studied by Jiang et al. (2006). Since disturbed (undisturbed) polar vortex conditions manifest as weakened (strengthened) background wind speeds, which in turn control the visibility of GWs to MLS (Alexander, 1998), much of the interannual variation in Fig. 9 may be a visibility effect controlled by interannual variations in the strength of vortex winds. For example, the northern winter stratosphere in February 2006 experienced a major warming that led to extremely weak stratospheric zonal-mean zonal wind speeds compared to more typical conditions in February 2005, which may explain via GW visibility arguments the smaller northern polar winter MLS variances in 2005 compared to 2006 in Fig. 9. However, analysis of SABER temperature data and global modeling by Siskind et al. (2007) suggest that the weakened 2006 vortex filtered out most orographic gravity waves, yielding much reduced upper-level orographic gravity wave drag relative to 2005, which then led to an anomalously strong lower-mesospheric vortex in 2006. Reductions in stratospheric GW temperature variances during stratospheric warmings have also

been reported in ground-based studies (e.g., Whiteway and Carswell, 1994). Thus the relative roles of wind filtering and real changes in stratospheric GW activity in forming the interannual GW variances in Fig. 9 during northern polar winter merit further investigation, and will be a focus of future research.

5 Comparisons with ECMWF Analyses

To help assess some of our inferences about the sensitivity of Aura MLS to different GW wavelengths, sources and propagation directions, we utilize as preliminary modeling support some high-resolution global analysis fields issued operationally by ECMWF IFS. We use global fields at the native T_L799L91 model resolution, corresponding to ~25 km horizontal gridpoint resolution on the reduced linear Gaussian grid. The 91 vertical model layers have a resolution of ~0.4 km in the lower stratosphere, increasing to ~1 km near ~30 km altitude and ~2 km at ~45 km altitude.

To first order, these nominal horizontal and vertical gridpoint resolutions act like the 3D WFs for Aura MLS in determining which GWs ECMWF IFS fields can and cannot explicitly simulate (the precise sensitivities to GWs are much more complex, depending on other model specifics, such as the amount of spectral hyperdiffusion applied to model divergence fields in the stratosphere). Thus, like MLS, the ECMWF IFS will tend to resolve GWs better in strong wind environments where vertical wavelengths become long. Indeed, earlier lower-resolution versions of ECMWF IFS forecast/analysis fields have revealed explicitly resolved gravity waves in the stratosphere within strong winds located near the polar vortex edge associated with orography (e.g., Hertzog et al., 2002; Eckermann et al., 2006a, 2006b; Alexander and Teitelbaum, 2007) and jet stream instabilities (Hertzog et al., 2001; Plougonven and Teitelbaum, 2003). Thus, these

higher resolution IFS fields should resolve even more stratospheric GW activity.

We begin by studying the analyzed ECMWF IFS temperature fields at one particular day and time (21 August 2006, 0000 UTC). We remove wave components with horizontal scales longer than ~ 300 km, to roughly mimic maximum resolved scales in the 40-pt MLS variances. No vertical filtering is applied in this initial analysis, which may produce larger GW variances than in the MLS variances by retaining GWs with vertical wavelengths that MLS either cannot resolve or resolves with significantly reduced amplitude due to WF smearing. However, since the IFS vertical resolution is ~ 2 km at 45 km altitude, the model fields here cannot resolve GWs with vertical wavelengths shorter than ~ 4 -6 km. Thus the IFS fields at 45 km have an intrinsic short- λ_z cutoff that is similar to the MLS 40-pt variances (see Fig. 3a).

Fig. 10 shows a global map of the instantaneous IFS temperature perturbation oscillations at ~ 44 km pressure altitude (assuming a constant scale height of 6.95 km), while Fig. 11 plots latitude-height cross sections of these oscillations at selected longitudes marked with dotted lines in Fig. 10. As with the Aura MLS variances in Figs. 5 and 7, the perturbation amplitudes in Fig. 10 peak near the edge of the southern polar vortex and the northern subtropics, where background winds are strongest and GW vertical wavelengths are longest and thus easiest for the IFS to resolve. Near the southern vortex edge, enhanced-amplitude perturbations are evident over southern South America, the Antarctic Peninsula and New Zealand due to mountain waves, but significant enhancements also occur over broader regions of the Southern Ocean well away from any mountains. The cross sections in Fig. 11 show some of this GW activity emanating from tropopause altitudes, presumably radiated from tropospheric jet stream instabilities associated

with baroclinic storm systems that regularly form and propagate across the Southern Ocean (O’Sullivan and Dunkerton, 1995; Guest et al., 2000). The cross sections in Fig. 11 show that the explicitly simulated GWs at 40°-80°S from both the jet and mountain sources exhibit wave phases that tilt upwards towards the South Pole, consistent with the predominant southward GW group propagation directions inferred from MLS *A-D* variance difference maps in Figs. 5 and 7.

Enhanced ECMWF IFS temperature perturbation amplitudes in the northern subtropical upper stratosphere in Fig. 10 exhibit a shorter scale, more disorganized structure with less horizontal coherence, superficially consistent with episodic localized generation from deep tropospheric convection. For example, the cross section at 236°E in Fig. 11 shows weaker amplitude GWs radiated into the stratosphere at ~10-20°S, a region over open ocean off the west coast of Mexico where enhanced GW activity is seen in Fig. 10. Since tropical cyclones are known to be sources of stratospheric GWs (e.g., Sato, 1993; Chane-Ming et al., 2002; Kim et al., 2005), these GWs were presumably generated in the IFS by Hurricane Hector, whose eye was near (18.3°N, 229°E) at this time and thus directly beneath the GW activity in Fig. 10.

Fig. 12b plots a map of the monthly mean analyzed ECMWF IFS temperature variance at 44 km pressure altitude in August, 2006, while Fig. 12a above it shows the corresponding 40-pt Aura MLS ascending radiance variance at ~44 km. There is general agreement between the two maps in terms of both geographical variability and variance level. As in MLS, the wave variances from the T_L799L91 analyses are enhanced in two distinct latitude bands where strong background winds increase the probability of MLS-resolvable GW vertical wavelengths in the stratosphere. The longitudinal modulation of the GW variances in these latitude bands suggests a non-uniform distribution of GW sources. For example, in the high-latitude southern band, mountain waves

from the southern Andes are the most prominent feature in Fig. 12b, as they are in the GW variances from Aura MLS (Fig. 12a) and those derived from other satellite instruments. The orographic GWs from the southern Andes propagate with large amplitudes thousands of kilometers downstream, as was observed from satellite and modeled by Preusse et al. (2002).

A band of enhanced IFS variance also occurs in the northern subtropics in Fig. 12b, with variance peaks occurring over southern U.S./Mexico and southeast Asia, features also seen in the Aura MLS GW variances in Fig. 12a (see also Fig. 7). The subtropical GW variance band from ECMWF IFS is slightly narrower latitudinally and displaced equatorward of the Aura MLS band. These differences may be related to slightly different GW vertical and horizontal wavelength sensitivities in each data set, or to the IFS's convectively-generated tropical GW spectrum, whose properties in global models prove highly sensitive to the way in which deep cumulus convection is parameterized (e.g., Horinouchi et al., 2003).

The overall similarities in Fig. 12 highlight the global GW resolving capabilities of both high-resolution satellite remote sensors like Aura MLS and high-resolution global models, like the T_L799L91 ECMWF IFS. Such comparisons illustrate the potential benefits of these Aura MLS GW data for validating the stratospheric GWs explicitly simulated and parameterized in global models.

6 Summary and Future Work

In this investigation, we have characterized the sensitivity of Aura MLS saturated 118 GHz radiances to stratospheric GWs of different wavelengths, and have used these insights to interpret

the GW-induced radiance perturbations that are located at the bottom of each normal limb scan. We have shown that small-scale perturbations in these saturated radiances are produced by horizontally-varying GW-induced temperature oscillations within a broad vertical atmospheric layer whose mean pressure altitude varies from ~ 21.7 km for channels 1 and 25, to ~ 51 km for channels 12 and 14. Vertical and along-track smearing by the MLS WFs (weighting functions) limit the instrument's sensitivity to GWs. Forward modeling shows that MLS has greatest sensitivity to high frequency GWs with short horizontal and long vertical wavelengths that propagate towards the instrument. This leads to anisotropy between GW variances measured on ascending and descending orbits, from which one can infer preferred northward or southward GW propagation components. The much narrower vertical FOV (field of view) and smaller channel noise of Aura MLS yield much improved sensitivity to GWs of all scales compared to the UARS MLS, particularly to GWs of shorter vertical wavelength. Aura MLS also provides variance data in the altitude region 21-28 km that was not covered by the UARS MLS thermal radiance channels. By extending the analysis to MLS 118 GHz channels located farther from and closer to the O_2 line center, it will be possible in future studies to observe GW variances at pressure altitudes down to ~ 15 km and up to ~ 95 km, respectively.

We used these capabilities to study GWs by first forming variances using the 40 saturated radiances located at the bottom of each limb scan, which yielded global data at twelve independent altitudes between 21 and 51 km. Aura MLS data acquired between late 2004 and mid-2007 were processed in this way and analyzed as a function of time, altitude and geographical location. The main findings were as follows:

1. The variances at 21-28 km altitude are enhanced at the tropics, as observed in GWs

resolved by high vertical-resolution satellite limb sounders and suborbital profilers.

2. These tropical GW variances show significant variations with QBO phase that agree with long-term tropical GW variances measured by sondes. The enhanced tropical MLS GW variance at 21.7 km is split into twin-peaked subtropical bands during the westerly (eastward) QBO wind phase, then reverts to a single strong equatorial peak during the easterly (westward) QBO phase.
3. Antarctic GW variances at 21-25 km altitude peak during October-November, while at higher altitudes they peak in mid-winter. These findings agree with radiosonde and GPS data from this region.
4. The variances in the upper stratosphere are similar in morphology to those from the UARS MLS, with seasonal and latitudinal enhancements correlating strongly with related increases in background wind speeds that refract GWs to the long vertical wavelength scales needed for MLS to resolve them (e.g., Alexander, 1998).
5. Longitudinal asymmetries reveal sources, such as strong orographic GW activity over the Andes, Antarctic Peninsula, New Zealand, Alaska, Scandinavia, Greenland, the Alps, Appalachians and Rockies during winter. Localized regions of enhanced tropical and subtropical variance correlate well with enhanced convection (diagnosed using the MLS cloud ice product) over the maritime continent, South America, southern Asia and the southeastern U.S. Preferred meridional components of propagation for GWs in all these regions were inferred from the differences in variance measured on ascending and descending orbits.

We briefly compared the GW variances observed by MLS in August 2006 to the explicitly resolved GW temperature oscillations in the T_L799L91 ECMWF IFS analyses at a pressure altitude of ~44 km. The monthly mean variance maps showed many similarities, including latitudinal bands of enhanced variance in regions of high background wind speed, and over regions of enhanced orographic and convective GW forcing. These comparisons highlight the potentially valuable role that Aura MLS GW observations can play in validating both the explicitly simulated GWs in very high-resolution models and those parameterized in low-resolution climate-chemistry models. More detailed model-observation comparisons require forward modeling of 3-D model temperature fields using the Aura MLS 3D WFs and in-orbit sampling patterns (e.g., Jiang et al., 2004a; Eckermann and Wu, 2006; Eckermann et al., 2006b), which we will explore in future work.

Future studies will also analyze GW perturbations in other MLS radiance channels that have better vertical resolution in the lower stratosphere. For example, MLS 240 and 640 GHz radiances have vertical FOVs of 3.2 and 1.4 km, respectively, at the tangent point, but the measurement noise at these frequencies is, respectively, 1.3 and 3.5 times larger than the 118 GHz measurements. Despite these larger noise variances, the improved sensitivity to the 2-4 km vertical wavelength GWs that dominate lower stratospheric GW variance (Allen and Vincent, 1995) may well yield significantly higher signal-to-noise ratios (SNRs) for GW variances at these altitudes. In addition, we can increase the SNR by employing a longer horizontal truncation length for the GW variance calculation (e.g., Jiang et al., 2002). This is potentially attractive for resolving the low-frequency GWs with long horizontal but short vertical wavelengths that dominate equatorial variances (Sato and Dunkerton, 1997; Vincent and Alexander, 2000;

Alexander et al., 2002; Ern et al., 2004; Wang et al., 2005). A long truncation length can be obtained by analyzing MLS radiances from adjacent limb scans that are separated by ~ 165 km. By binning 3-4 adjacent scans of MLS radiances, we will be able to increase the cutoff horizontal wavelengths to 500-600 km. For all the GW studies extended to long horizontal wavelengths, however, we need to be careful not to alias in planetary waves (e.g., Kelvin or mixed Rossby-gravity waves). Inability to distinguish GWs from planetary waves, which often have vertical wavelengths as short as 3-4 km, has been an issue with GW observations from radiosondes, rocketsondes and other satellite limb techniques (e.g., Eckermann, 1995).

Acknowledgments

This work was supported by NASA program NNH04ZYS004N (“Measurements Modeling and Analyses in Support of Aura and Other Satellite Observations of the Earth’s Atmosphere”). DLW’s research was performed at the Jet Propulsion Laboratory (JPL), California Institute of Technology under contract with the National Aeronautics and Space Administration (NASA), and supported by NASA Aura project. SDE acknowledges additional support from NASA’s Geospace Sciences SR&T Program. We thank the UK Met Office for providing stratospheric wind analyses and the ECMWF for providing T_L799L91 IFS analysis data. Assistance from Dr. Evan Fishbein in accessing the ECMWF data is also acknowledged. Finally, we thank the JPL MLS team for successful instrument development, operation and data processing, and three anonymous reviewers for valuable comments on the original manuscript.

References

- Alexander, M. J., 1998: Interpretations of observed climatological patterns in stratospheric gravity wave variance, *J. Geophys. Res.*, **103**, 8627-8640.
- Alexander, M. J., and C. Barnet, 2007: Using satellite observations to constrain parameterizations of gravity wave effects for global models. *J. Atmos. Sci.*, **64**, 1652-1665
- Alexander, M. J., and H. Teitelbaum, 2007: Analysis and observation of a large amplitude mountain wave event over the Antarctic Peninsula, *J. Geophys. Res.*, doi:10.1029/2006JD008368, (in press).
- Alexander, M. J., T. Tsuda, and R. A. Vincent, 2002: Latitudinal variations observed in gravity waves with short vertical wavelengths, *J. Atmos. Sci.*, **59**, 1394-1404.
- Alexander, M. J., P. T. May, J. H. Beres, 2004: Gravity waves generated by convection in the Darwin area during the Darwin Area Wave Experiment, *J. Geophys. Res.*, **109** (D20), D20S04, doi:10.1029/2004JD004729.
- Allen, S. J., and R. A. Vincent, 1995: Gravity wave activity in the lower atmosphere: Seasonal and latitudinal variations. *J. Geophys. Res.*, **100**, 1327-1350.
- Bacmeister, J. T., S. D. Eckermann, P. A. Newman, L. Lait, K. R. Chan, M. Loewenstein, M. H. Proffitt, and B. L. Gary, 1996: Stratospheric horizontal wavenumber spectra of winds, potential temperature and atmospheric tracers observed by high-altitude aircraft, *J. Geophys. Res.*, **101**, 9441-9470.
- Baldwin, M. P., et al., 2001: The quasi biennial oscillation, *Rev. Geophys.*, **39**(2), 179-230.
- Baumgaertner, A. J. G., and A. J. McDonald, 2007: A gravity wave climatology for Antarctica compiled from Challenging Minisatellite Payload/Global Positioning System

- (CHAMP/GPS) radio occultations, *J. Geophys. Res.*, **112**, D05103, doi:10.1029/2006JD007504.
- Chane-Ming, F., G. Roff, L. Robert, and J. Leveau, 2002 : Gravity wave characteristics over Tromelin Island during the passage of cyclone Hudah, *Geophys. Res. Lett.*, **29**(6), 1094, doi:10.1029/2001GL013286.
- Cofield, R.E., and P.C.Stek, 2006: Design and field-of-view calibration of 114-660 GHz optics of the Earth Observing System Microwave Limb Sounder, *IEEE Trans. Geosci. Remote Sensing*, **44**, 1166-1181.
- de la Torre, A., T. Schmidt, and J. Wickert, 2006: A global analysis of wave potential energy in the lower stratosphere derived from 5 years of GPS radio occultation data with CHAMP, *Geophys. Res. Lett.*, **33**, L24809, doi:10.1029/2006GL027696.
- Eckermann, S. D., 1995: On the observed morphology of gravity-wave and equatorial-wave variance in the stratosphere, *J. Atmos. Terr. Phys.*, **57**, 105-134.
- Eckermann, S. D. and P. Preusse, 1999: Global measurements of stratospheric mountain waves from space, *Science*, **286**, 1534-1537.
- Eckermann, S. D., and D. L. Wu, 2006: Imaging gravity waves in lower stratospheric AMSU-A radiances, Part 1: Simple forward model, *Atmos. Chem. Phys.*, **6**, 3325-3341.
- Eckermann, S. D., I. Hirota, and W. K. Hocking, 1995: Gravity-wave and equatorial-wave morphology of the stratosphere derived from long-term rocket soundings, *Quart. J. Roy. Meteor. Soc.*, **121**, 149-186.
- Eckermann, S. D., A. Dörnbrack, S. B. Vosper, H. Flentje, M. J. Mahoney, T. P. Bui, and K. S. Carslaw, 2006a: Mountain wave-induced polar stratospheric cloud forecasts for aircraft

- science flights during SOLVE/THESEO 2000, *Wea. Forecasting*, **21**, 42-68.
- Eckermann, S. D., et al., 2006b: Imaging gravity waves in lower stratospheric AMSU-A radiances, Part 2: Validation case study, *Atmos. Chem. Phys.*, **6**, 3343-3362.
- Ern, M., P. Preusse, M. J. Alexander, and C. D. Warner, 2004: Absolute values of gravity wave momentum flux derived from satellite data, *J. Geophys. Res.*, **109**, D20103, doi:10.1029/2004JD004752.
- Fetzer, E. J., and J. C. Gille, 1994: Gravity wave variance in LIMS temperatures. Part I: Variability and comparison with background winds. *J. Atmos. Sci.*, **51**, 2461-2483.
- Fritts, D. C., and M. J. Alexander, 2003: Gravity wave dynamics and effects in the middle atmosphere. *Rev. Geophys.* **41** (1), 1003, doi:10.1029/2001RG000106.
- Fritts, D. C., S. L. Vadas, K. Wan, and J. A. Werne, 2006: Mean and variable forcing of the middle atmosphere by gravity waves, *J. Atmos. Sol.-Terr. Phys.*, **68**, 247-265.
- Guest, F. M., M. J. Reeder, C. J. Marks, and D. J. Karoly, 2000: Inertia-gravity waves observed in the lower stratosphere over Macquarie Island, *J. Atmos. Sci.*, **57**, 737-752.
- Hertzog, A., C. Souprayen, and A. Hauchecorne, 2001: Observation and backward trajectory of an inertio-gravity wave in the lower stratosphere, *Ann. Geophysicae*, **19**, 1141-1155.
- Hertzog, A., F. Vial, A. Dörnbrack, S. D. Eckermann, B. M. Knudsen, and J.-P. Pommereau, 2002: In-situ observations of gravity waves and comparisons with numerical simulations during the SOLVE/THESEO 2000 campaign, *J. Geophys. Res.*, **107**(D20), 8292, 10.1029/2001JD001025, 2002.
- Horinouchi, T., et al. (2003), Tropical cumulus convection and upward-propagating waves in middle-atmospheric GCMs, *J. Atmos. Sci.*, **60**, 2765-2782.

- Jarnot, R. F., R. E. Cofield, J. W. Waters, D. A. Flower, and D. E. Peckham, 1996: Calibration of the Microwave Limb Sounder on the Upper Atmosphere Research Satellite. *J. Geophys. Res.*, **101**, 9957–9982.
- Jiang, J.H., and D.L. Wu, 2001: UARS MLS observations of gravity waves associated with the Arctic winter stratospheric vortex, *Geophys. Rev. Lett.*, **28**, 527-530.
- Jiang, J.H., D.L. Wu, and S.D. Eckermann, 2002: Upper Atmosphere Research Satellite (UARS) MLS observation of mountain waves over the Andes. *J. Geophys. Res.*, **107**, 10.1029/2002JD002091.
- Jiang, J.H, S.D. Eckermann, D.L. Wu, and J. Ma, 2004a: A search for mountain waves in MLS stratospheric limb radiances from the winter northern hemisphere: data analysis and global mountain wave modeling, *J. Geophys. Res.* **109**, No. D3, D03107, 10.1029/2003JD003974.
- Jiang, J. H., B. Wang, K. Goya, K. Hocke, S.D. Eckermann, J. Ma, D.L. Wu, and W.G. Read, 2004b: Geographical distribution and interseasonal variability of tropical deep convection: UARS MLS observations and analyses. *J Geophys. Res.*, **109**, D03111, doi:10.1029/2003JD003756.
- Jiang, J. H., S. D. Eckermann, D. L. Wu, K. Hocke, B. Wang, J. Ma, and Y. Zhang, 2005: Seasonal variation of gravity wave sources from satellite observation, *Adv. Space Res.*, **35**, 1925-1932.
- Jiang, J. H., S. D. Eckermann, D. L. Wu, and, D.-Y. Wang, 2006: Interannual variation of gravity waves in the Arctic and Antarctic winter middle atmosphere, *Adv. Space Res.*, **38**, 2418-2423.

- Kim, Y.-J., S. D. Eckermann, and H.-Y. Chun, 2003: A overview of the past, present and future of gravity-wave drag parameterization for numerical climate and weather prediction models, *Atmos. Ocean*, **41**, 65-98.
- Kim, S.-Y., H.-Y. Chun, and J.-J. Baik, 2005: A numerical study of gravity waves induced by convection associated with Typhoon Rusa, *Geophys. Res. Lett.*, **32**, L24816, doi:10.1029/2005GL024662.
- Koshyk, J. N., and K. Hamilton, 2001: The horizontal kinetic energy spectrum and spectral budget simulated by a high-resolution troposphere–stratosphere–mesosphere GCM. *J. Atmos. Sci.*, **58**, 329–348.
- Krebsbach, M., and P. Preusse, 2007: Spectral analysis of gravity wave activity in SABER temperature data, *Geophys. Res. Lett.*, **34**, L03814, doi:10.1029/2006GL028040.
- Limpasuvan, V., D. L. Wu, M. J. Alexander, M. Xue, M. Hu, S. Pawson, and J. R. Perkins, 2007: Stratospheric gravity wave simulation over Greenland during 24 January 2005, *J. Geophys. Res.*, **112**, D10115, doi:10.1029/2006JD007823.
- McLandress, C., 1998: On the importance of gravity waves in the middle atmosphere and their parameterization in general circulation models, *J. Atmos. Sol. Terr. Phys.*, **60**, 1357–1383.
- McLandress, C., and J. F. Scinocca, 2005: The GCM response to current parameterizations of nonorographic gravity wave drag, *J. Atmos. Sci.*, **62**, 2394–2413.
- McLandress, C., M. J. Alexander, and D. L. Wu, 2000: Microwave limb sounder observations of gravity waves in the stratosphere: a climatology and interpretation, *J. Geophys. Res.*, **105**, 11947-11967.
- O’Sullivan, D., and T. J. Dunkerton, 1995: Generation of inertia-gravity waves in a

- simulated life cycle of baroclinic instability, *J. Atmos. Sci.*, **52**, 3695–3715.
- Pfenninger, M., A. Z. Liu, G. C. Papen, and C. S. Gardner, 1999: Gravity wave characteristics and in the lower atmosphere at South Pole, *J. Geophys. Res.*, **104**, 5963-5984.
- Plougonven, R., and H. Teitelbaum, 2003: Comparison of a large-scale inertia-gravity wave as seen in the ECMWF analyses and from radiosondes, *Geophys. Res. Lett.*, **30**(18), 1954, doi:10.1029/2003GL017716.
- Preusse, P., S. D. Eckermann and D. Offermann, 2000: Comparison of global distributions of zonal-mean gravity wave variance inferred from different satellite instruments. *Geophys. Res. Lett.*, **27**, 3877-3880.
- Preusse, P., A. Dörnbrack, S. D. Eckermann, M. Riese, B. Schaeler, J. T. Bacmeister, D. Broutman, and K. U. Grossmann, 2002: Space-based measurements of stratospheric mountain waves by CRISTA - 1. Sensitivity, analysis method, and a case study. *J. Geophys. Res.*, **107** (D23), 8178, doi:10.1029/2001JD000699..
- Preusse, P. et al., 2006: Tropopause to mesopause gravity waves in August: Measurement and modeling. *J. Atmos. Solar-Terr. Phys.*, **68**, 1730-1751, 2006.
- Randel, W. J., and F. Wu, 2005: Kelvin wave variability near the equatorial tropopause observed in GPS radio occultation measurements. *J. Geophys. Res.*, **110**, D03102, doi:10.1029/2004JD005006.
- Ratnam, M. V., G. Tetzlaff, and C. Jacobi, 2004: Global and seasonal variations of stratospheric gravity wave activity deduced from the *CHAMP*/GPS satellite, *J. Atmos. Sci.*, **61**, 1610-1620.

- Read, W. G., Z. Shippony, M. J. Schwartz, N. J. Livesey, and W. Van Snyder, 2006: The clear-sky unpolarized forward model for the EOS Aura Microwave Limb Sounder (MLS), *IEEE Trans. Geosci. Remote Sens.*, **44**, 1367–1379.
- Sato, K., 1993: Small-scale wind disturbances observed by the MU radar during the passage of typhoon Kelly, *J. Atmos. Sci.*, **50**, 518–537.
- Sato, K., and T. J. Dunkerton, 1997: Estimates of momentum flux associated with equatorial Kelvin and gravity waves, *J. Geophys. Res.*, **102**, 26,247-26,261.
- Siskind, D. E., S. D. Eckermann, L. Coy, J. P. McCormack, and C. E. Randall, 2007: On recent interannual variability of the Arctic winter mesosphere: implications for tracer descent, *Geophys. Res. Lett.*, **34**, L09806, doi:10.1029/2007GL029293 .
- Tsuda, T., T. E. VanZandt, M. Mizumoto, S. Kato, and S. Fukao, 1991: Spectral analysis of temperature and Brunt-Väisälä frequency fluctuations observed by radiosondes, *J. Geophys. Res.*, **96**, 17265-17278.
- Tsuda, T., M. Nishida, C. Rocken, and R. H. Ware, 2000: A global morphology of gravity wave activity in the stratosphere revealed by the GPS occultation data (GPS/MET), *J. Geophys. Res.*, **105**, 7257-7273.
- Tsuda, T., M. V. Ratnam, P. T. May, M. J. Alexander, R. A. Vincent, and A. MacKinnon, 2004: Characteristics of gravity waves with short vertical wavelengths observed with radiosonde and GPS occultation during DAWEX (Darwin Area Wave Experiment), *J. Geophys. Res.*, **109**, D20S03, doi:10.1029/2004JD004946.
- Vincent, R. A., and M. J. Alexander, 2000: Gravity waves in the tropical lower stratosphere: An observational study of seasonal and interannual variability, *J. Geophys. Res.*, **105**,

17,971–17,982.

Wang, L., 2003: Gravity wave analysis of four years of high vertical resolution U.S. radiosonde data, Ph.D. thesis, Stony Brook Univ., New York.

Wang, L., and M. A. Geller, 2003: Morphology of gravity-wave energy as observed from 4 years (1998–2001) of high vertical resolution U.S. radiosonde data, *J. Geophys. Res.*, **108**(D16), 4489, doi:10.1029/2002JD002786.

Wang, L., M. A. Geller, and M. J. Alexander, 2005: Spatial and temporal variations of gravity wave parameters. Part I: Intrinsic frequency, wavelength, and vertical propagation direction, *J. Atmos. Sci.*, **62**, 125–142.

Waters, J. W., et al., 2006: The Earth Observing System Microwave Limb Sounder (EOS MLS) on the Aura satellite, *IEEE Trans. Geosci. Remote Sens.*, **44**, 1075–1092.

Whiteway, J. A., 1999: Enhanced and inhibited gravity wave spectra, *J. Atmos. Sci.*, **56**, 1344–1352.

Whiteway, J. A., and A. I. Carswell, 1994: Rayleigh lidar observations of thermal structure and gravity wave activity in the high Arctic during a stratospheric warming, *J. Atmos. Sci.*, **51**, 3122–3136.

Wu, D. L., 2001: Horizontal wavenumber spectrum of MLS radiances, *J. Atmos. Solar-Terr. Phys.*, **63**, 1465–1477.

Wu, D. L., 2004: Mesoscale gravity wave variances from AMSU-A radiances. *Geophys. Res. Lett.*, L12114, doi:10.1029/2004GL019562.

Wu, D. L., 2006: Small-scale fluctuations and scintillations in high-resolution GPS SNR and phase data, *J. Atmos. Sol.-Terr. Phys.*, **68**, 999–1017..

- Wu, D. L., and J. W. Waters, 1996: Satellite observations of atmospheric variances: A possible indication of gravity waves, *Geophys. Res. Lett.*, **23**, 3631-3634.
- Wu, D. L., and J. W. Waters, 1997: Observations of gravity waves with the UARS Microwave Limb Sounder, *Gravity Wave Processes*, NATO ASI Series I: *Global Environmental Change*, **50**, 103-120.
- Wu, D. L., and F. Zhang, 2004: A study of mesoscale gravity waves over the North Atlantic with satellite observations and a mesoscale model, *J. Geophys. Res.* **109**, D22104, doi:10.1029/2004JD005090.
- Wu, D. L., P. Preusse, S. D. Eckermann, J. H. Jiang, M. de la Torre Juarez, L. Coy, and D. Y. Wang, 2006a: Remote sounding of atmospheric gravity waves with satellite limb and nadir techniques, *Adv. Space Res.*, **37**, 2269-2277.
- Wu, D. L., J. H. Jiang, C. Davis, 2006b: EOS MLS cloud ice measurements and radiative transfer model, *IEEE Trans. Geosci. Remote Sens.*, **44**, 1156-1165.
- Yoshiki, M., and K. Sato, 2000: A statistical study of gravity waves in the polar regions based on operational radiosonde data, *J. Geophys. Res.*, **105**, 17,995-18,011.
- Yoshiki, M., N. Kizu, and K. Sato, 2004: Energy enhancements of gravity waves in the Antarctic lower stratosphere associated with variations in the polar vortex and tropospheric disturbances, *J. Geophys. Res.*, **109**, D23104, doi:10.1029/2004JD004870.

Figures

Figure 1. MLS horizontally-integrated temperature weighting functions (left), limb radiance profiles (middle), and saturated radiance perturbations (right) from a scan over northern tip of Antarctic Peninsula (55°W, 63°S) at 04:02:48 UTC on 2 September 2004. The weighting functions represent the derivatives of the saturated radiance with respect to atmospheric temperature (Read et al., 2006), and provide 12 distinct layers from the 25 channels (excluding channel 13). The straight line in the middle panel separates (roughly) saturated and unsaturated radiances. The perturbations in the right panel are the same radiance perturbations at low tangent heights as in the middle panel, except that they are plotted as a function of latitude (see text). The phase of perturbations is shifted with respect to altitude. The latitude of these radiances reflects the actual location where saturation takes place.

Figure 2. (a) A schematic diagram of an MLS scan, showing the 2-D cross sections through the 3-D temperature weighting functions (WFs; gray-shaded cigar-like volume) of saturated limb radiances with respect to wave propagation structures (dark gray linear phase lines). The Aura MLS flight direction is indicated by the short thick arrow. As MLS scans vertically, the peak altitudes of these WFs of the saturated radiances change very little, but the WFs are displaced horizontally as shown, giving unique sensitivity to the horizontal structure of gravity waves propagating in the saturation layer (dotted line). (b) An example of the Aura MLS sampling track. The LOS viewing angles with respect to the meridian are indicated on the right as a function of latitude.

Figure 3. MLS GW visibility function for the 40-pt variance calculation (a) as a function of along-track wavelength λ_v and vertical wavelength λ_z ; (b) as a function of λ_z/λ_v ratio and λ_z . Contour labels are radiance variances (in K^2) for an input GW peak amplitude of 1 K (variance of 0.5 K^2). See text for further details.

Figure 4. Latitude-height distribution of zonal-mean MLS GW variance from (a) ascending and (b) descending

orbits for January 2005. Contours are the zonal mean zonal winds from the UK Met Office analysis (dotted westward, solid eastward, contour labels in meters per second) and the bold dotted line is the simultaneous MLS ice water content (IWC) with the scale on the right axis. (c) Zonal-mean GW variance differences between ascending and descending orbits. The overplotted white lines depict schematically the wave phase orientation inferred from the statistically-significant A-D variance differences (southward for $A-D > 0$ and northward for $A-D < 0$).

Figure 5. As in Fig.4 but for July 2005.

Figure 6. MLS GW variance maps for January 2005, showing ascending (left), descending (middle), and ascending-descending (A-D) differences (right) for selected channels. The white contours are 5 mg/m^3 of MLS IWC as an indicator of deep convective forcing. Both ascending and descending maps share the same color scale, whereas the A-D maps use the scale to the right.

Figure 7. MLS GW variance maps for July 2005, showing ascending (left), descending (middle), and ascending-descending (A-D) differences (right) for selected pressure altitudes. The white contours are 5 mg/m^3 of MLS IWC as an indicator of deep convective forcing. Both ascending and descending maps share the same color scale, whereas the A-D maps use the scale to the right.

Figure 8. Monthly maps of the ascending (A), descending (D), and A-D variances at $\sim 21.7 \text{ km}$ pressure altitude for 2006. The color scales, ranges and contours have their same values and meaning as the 21.7 km altitude panels in Figures 6-7.

Figure 9. Time series of monthly zonal-mean ascending (A), descending (D), and A-D variances at selected altitudes. Color scales and units for A and D variances are given by the common color bar between each panel, and for A-D variances by the color bar to the far right. The tick marks associated with year label on the time axis indicate the beginning of that year. Overlaid contours depict the mean zonal wind from the UKMO analysis at intervals of 20 m/s , with dashed (solid) lines indicating westward (eastward) winds.

Figure 10. Temperature perturbation map from the ECMWF T_L799L91 analysis fields at 44 km pressure altitude at 0000 UTC on 20 August 2006. Color scale has units of Kelvin. A 2D horizontal high-pass filter was applied to extract small-scale structure, which corresponds to a long wavelength cutoff of ~300 km at low and middle latitudes. Dotted lines indicate the cross sections to be shown in Fig. 11 at 82°E, 171°E, 236°E and 297°E longitudes.

Figure 11. Cross-sections of temperature perturbations (in Kelvin, see color bars) as a function of latitude and pressure altitude from the ECMWF T_L799L91 analysis fields on 20 August 2006 at 0000 UTC at the selected longitudes shown in the title (in degrees east) and highlighted in Fig. 10. Contours lines are the background zonal winds from the ECMWF IFS analysis at that longitude and have increments of 10 m/s with dashed (solid) lines denoting westward (eastward) values.

Figure 12. Map of monthly-mean GW temperature variance at ~44 km pressure altitude from (a) Aura MLS GW variance from Channels 11/15, and (b) ECMWF IFS T_L799L91 analyses for every day of August 2006. As in Figs. 10-11, temperature perturbations in the ECMWF IFS analyses were truncated to exclude horizontal wavelengths > ~300 km before the variance was computed, but no vertical filter was applied.

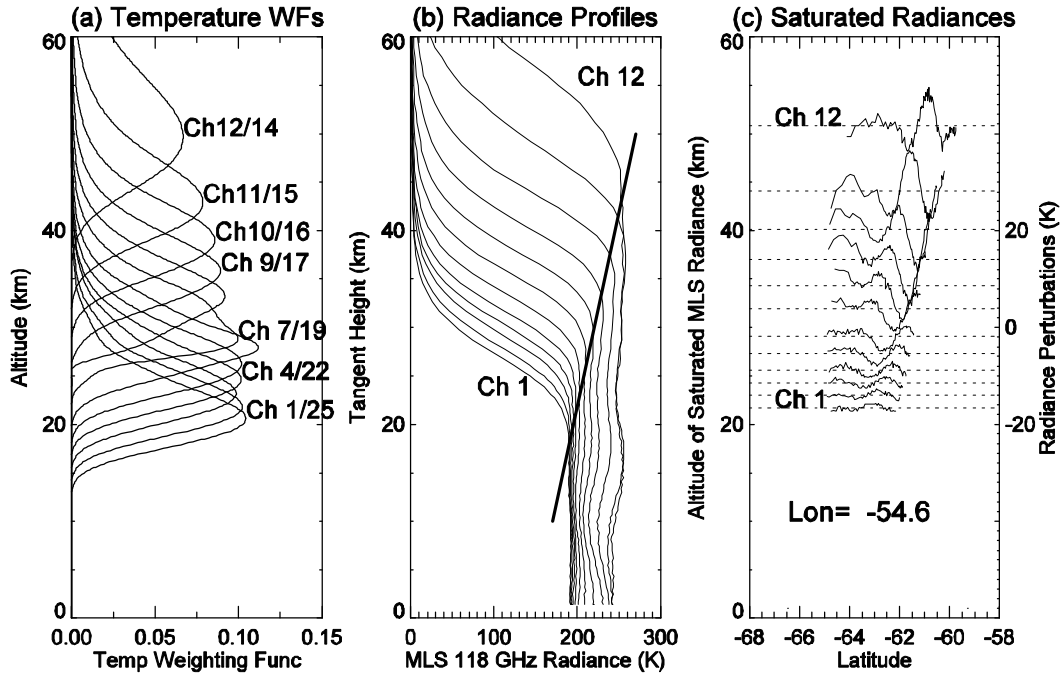


Figure 1. MLS horizontally-integrated temperature weighting functions (left), limb radiance profiles (middle), and saturated radiance perturbations (right) from a scan over northern tip of Antarctic Peninsula (55°W , 63°S) at 04:02:48 UTC on 2 September 2004. The weighting functions represent the derivatives of the saturated radiance with respect to atmospheric temperature (Read et al., 2006), and provide 12 distinct layers from the 25 channels (excluding channel 13). The straight line in the middle panel separates (roughly) saturated and unsaturated radiances. The perturbations in the right panel are the same radiance perturbations at low tangent heights as in the middle panel, except that they are plotted as a function of latitude (see text). The phase of perturbations is shifted with respect to altitude. The latitude of these radiances reflects the actual location where saturation takes place.

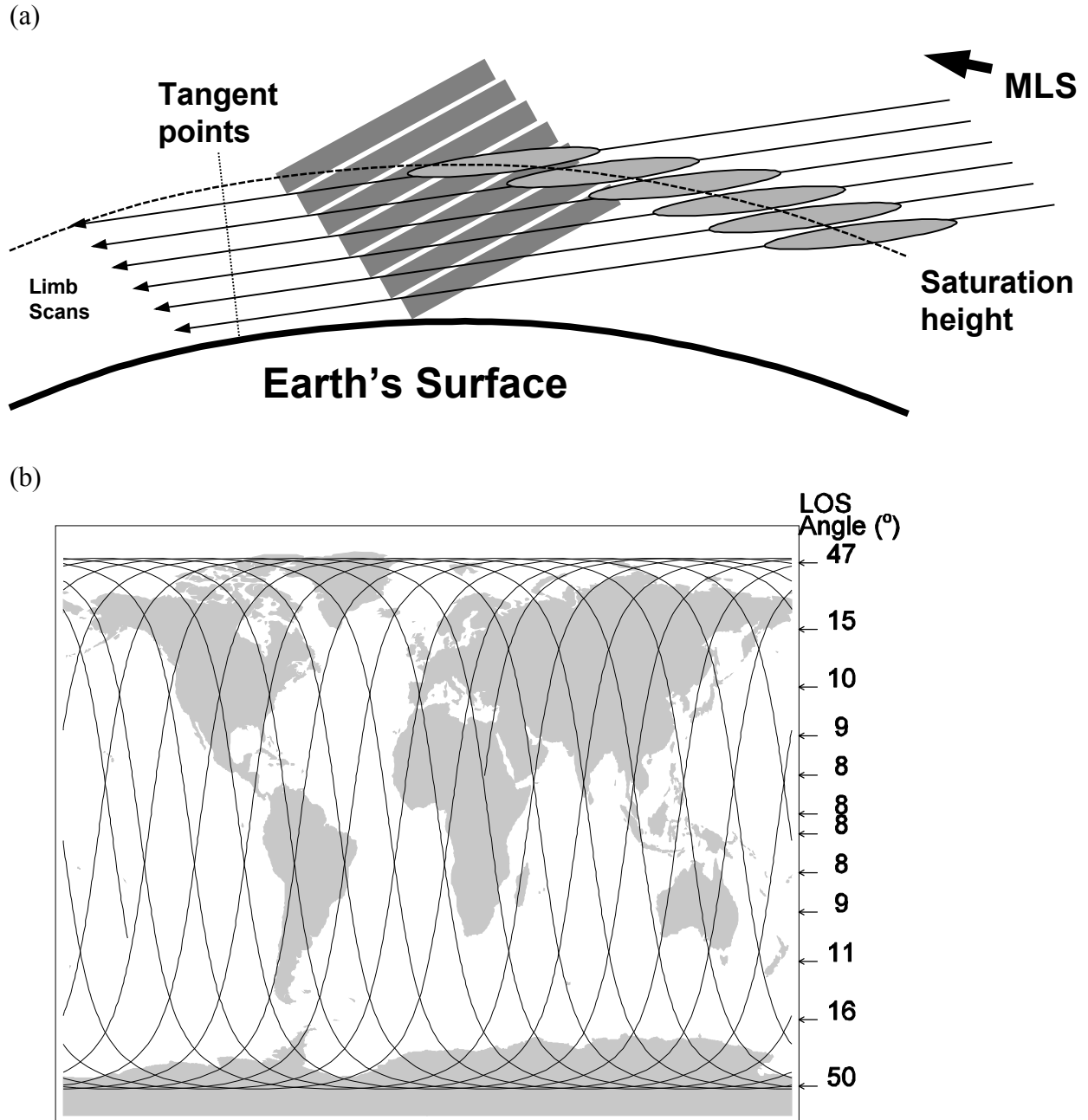


Figure 2. (a) A schematic diagram of an MLS scan, showing the 2-D cross sections through the 3-D temperature weighting functions (WFs; gray-shaded cigar-like volume) of saturated limb radiances with respect to wave propagation structures (dark gray linear phase lines). The Aura MLS flight direction is indicated by the short thick arrow. As MLS scans vertically, the peak altitudes of these WF of the saturated radiances change very little, but the WF are displaced horizontally as shown, giving unique sensitivity to the horizontal structure of gravity waves propagating in the saturation layer (dotted line). (b) An example of the Aura MLS sampling track. The LOS viewing angles with respect to the meridian are indicated on the right as a function of latitude.

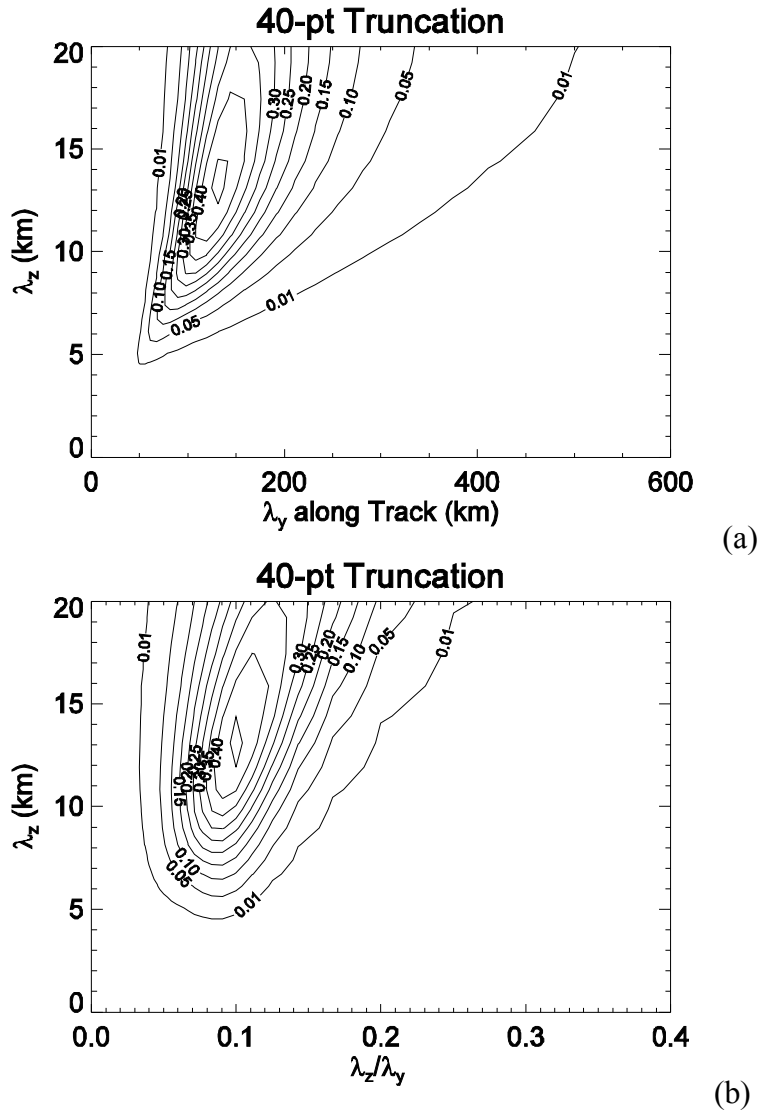


Figure 3. MLS GW visibility function for the 40-pt variance calculation (a) as a function of along-track wavelength λ_y and vertical wavelength λ_z ; (b) as a function of λ_z/λ_y ratio and λ_z . Contour labels are radiance variances (in K^2) for an input GW peak amplitude of 1 K (variance of $0.5 K^2$). See text for further details.

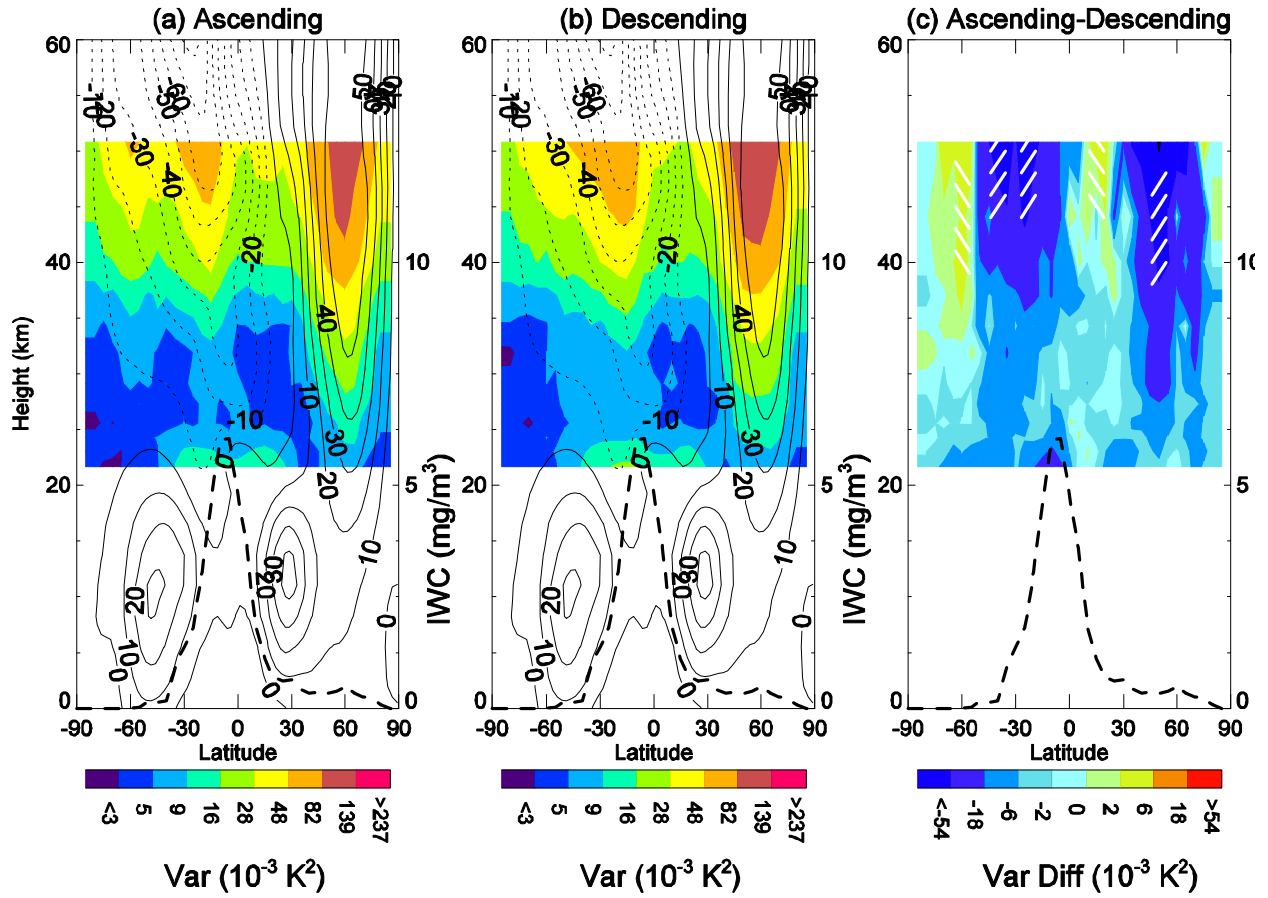


Figure 4. Latitude-height distribution of zonal-mean MLS GW variance from (a) ascending and (b) descending orbits for January 2005. Contours are the zonal mean zonal winds from the UK Met Office analysis (dotted westward, solid eastward, contour labels in meters per second) and the bold dotted line is the simultaneous MLS ice water content (IWC) with the scale on the right axis. (c) Zonal-mean GW variance differences between ascending and descending orbits. The overplotted white lines depict schematically the wave phase orientation inferred from the statistically-significant A-D variance differences (southward for $A-D > 0$ and northward for $A-D < 0$).

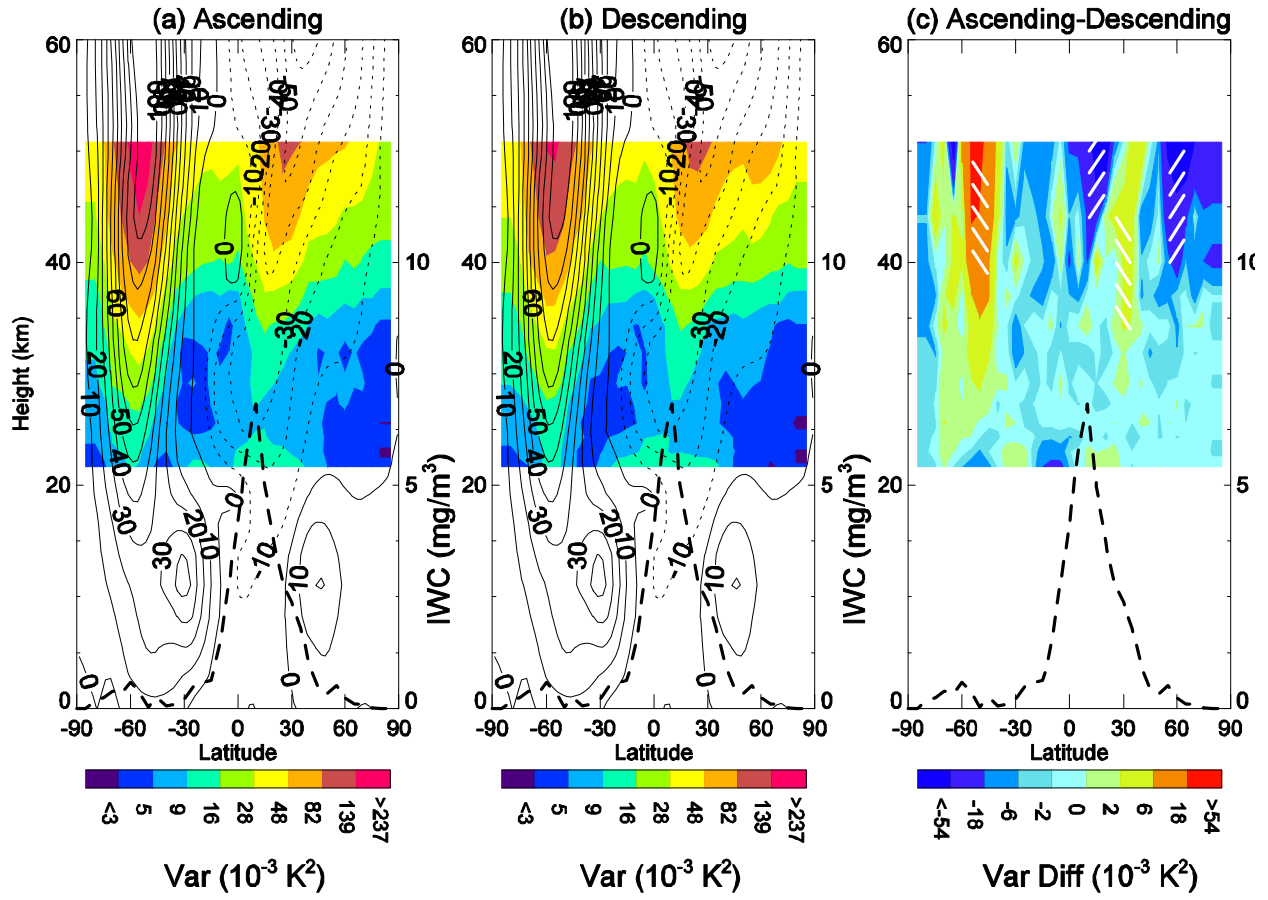


Figure 5. As in Fig.4 but for July 2005.

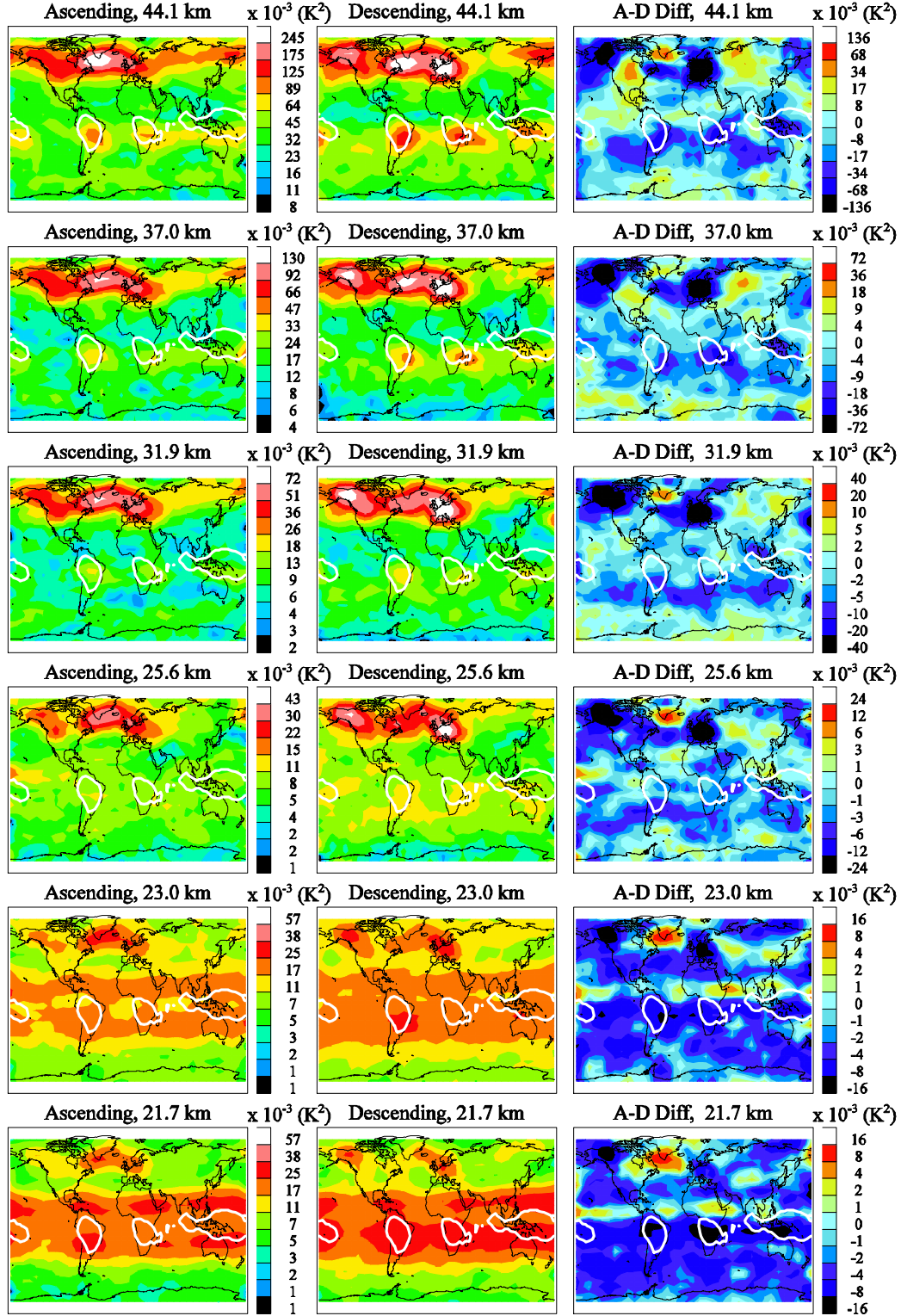


Figure 6. MLS GW variance maps for January 2005, showing ascending (left), descending (middle), and ascending-descending (A-D) differences (right) for selected channels. The white contours are 5 mg/m³ of MLS IWC as an indicator of deep convective forcing. Both ascending and descending maps share the same color scale, whereas the A-D maps use the scale to the right.

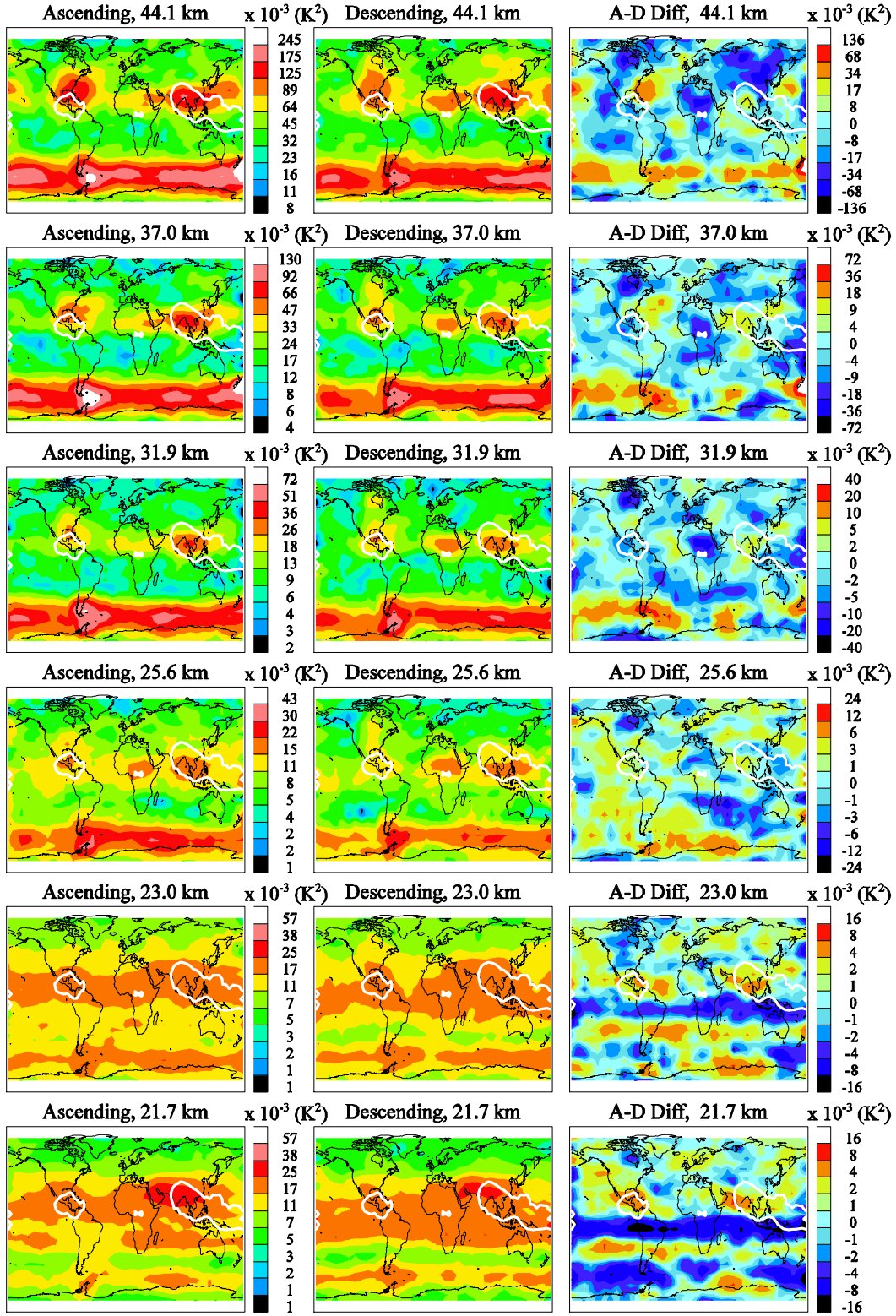


Figure 7. MLS GW variance maps for July 2005, showing ascending (left), descending (middle), and ascending-descending (A-D) differences (right) for selected pressure altitudes. The white contours are 5 mg/m^3 of MLS IWC as an indicator of deep convective forcing. Both ascending and descending maps share

the same color scale, whereas the A-D maps use the scale to the right.

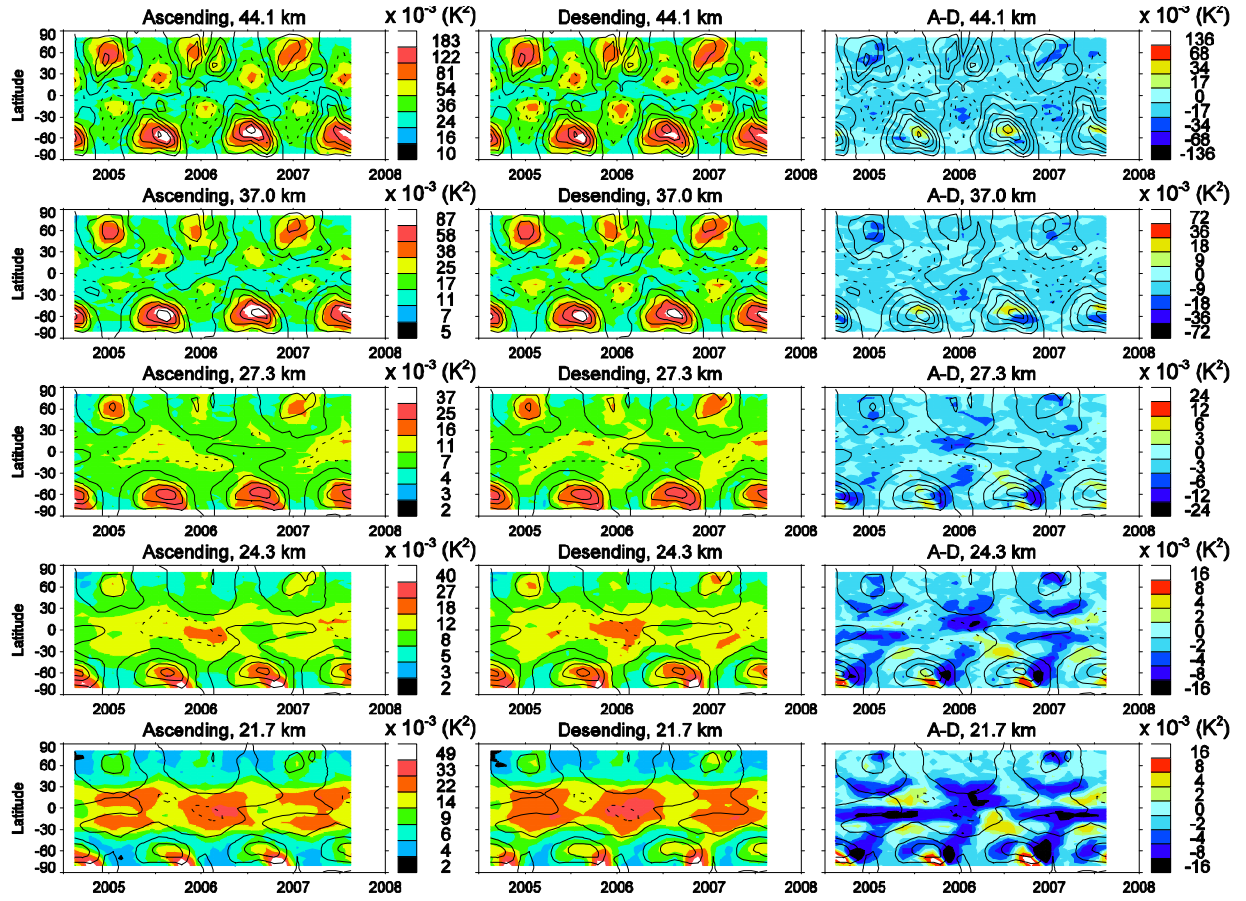


Figure 8. Monthly maps of the ascending (A), descending (D), and A-D variances at ~21.7 km pressure altitude for 2006. The color scales, ranges and contours have their same values and meaning as the 21.7 km altitude panels in Figures 6-7.

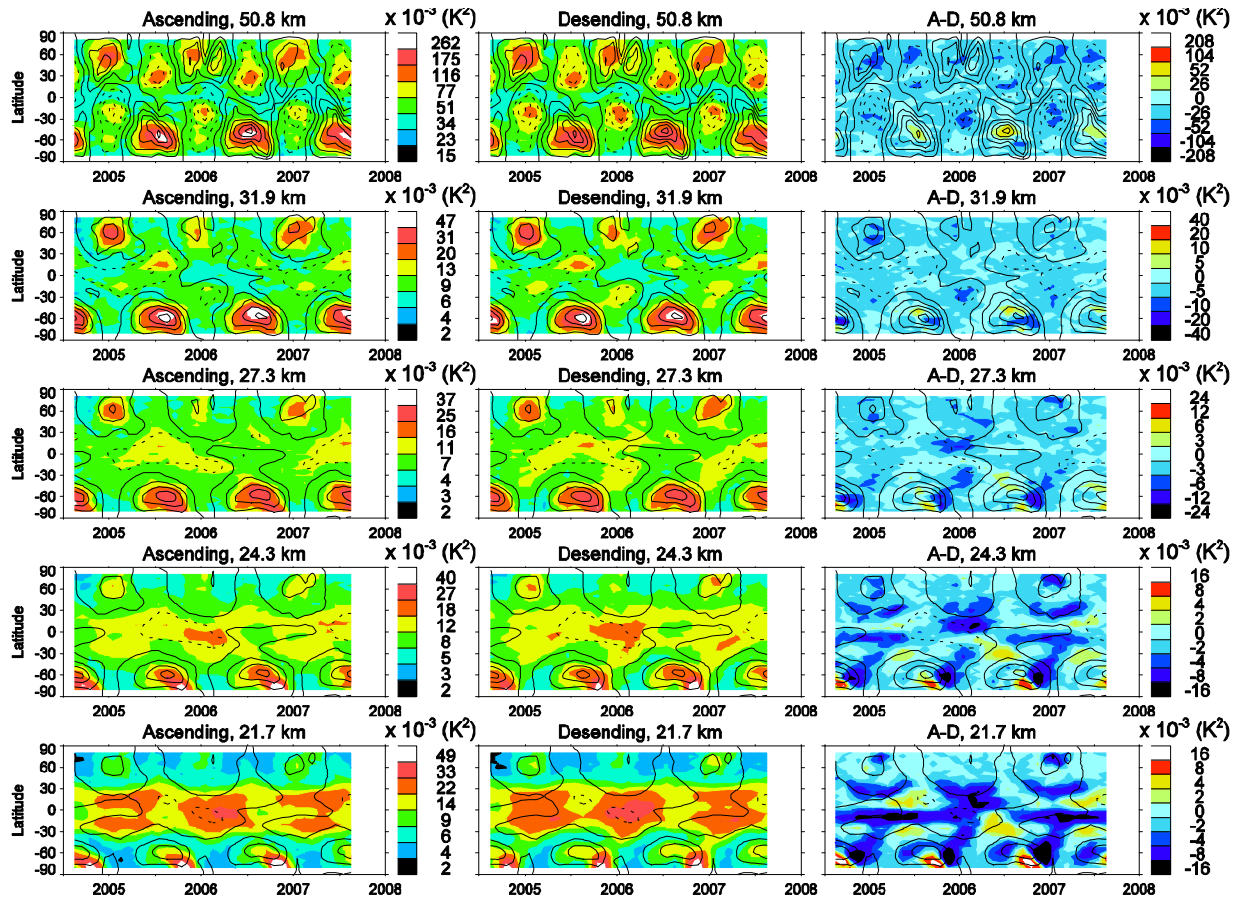


Figure 9. Time series of monthly zonal-mean ascending (A), descending (D), and A-D variances at selected altitudes. Color scales and units for A and D variances are given by the common color bar between each panel, and for A-D variances by the color bar to the far right. The tick marks associated with year label on the time axis indicate the beginning of that year. Overlaid contours depict the mean zonal wind from the UKMO analysis at intervals of 20 m/s, with dashed (solid) lines indicating westward (eastward) winds.

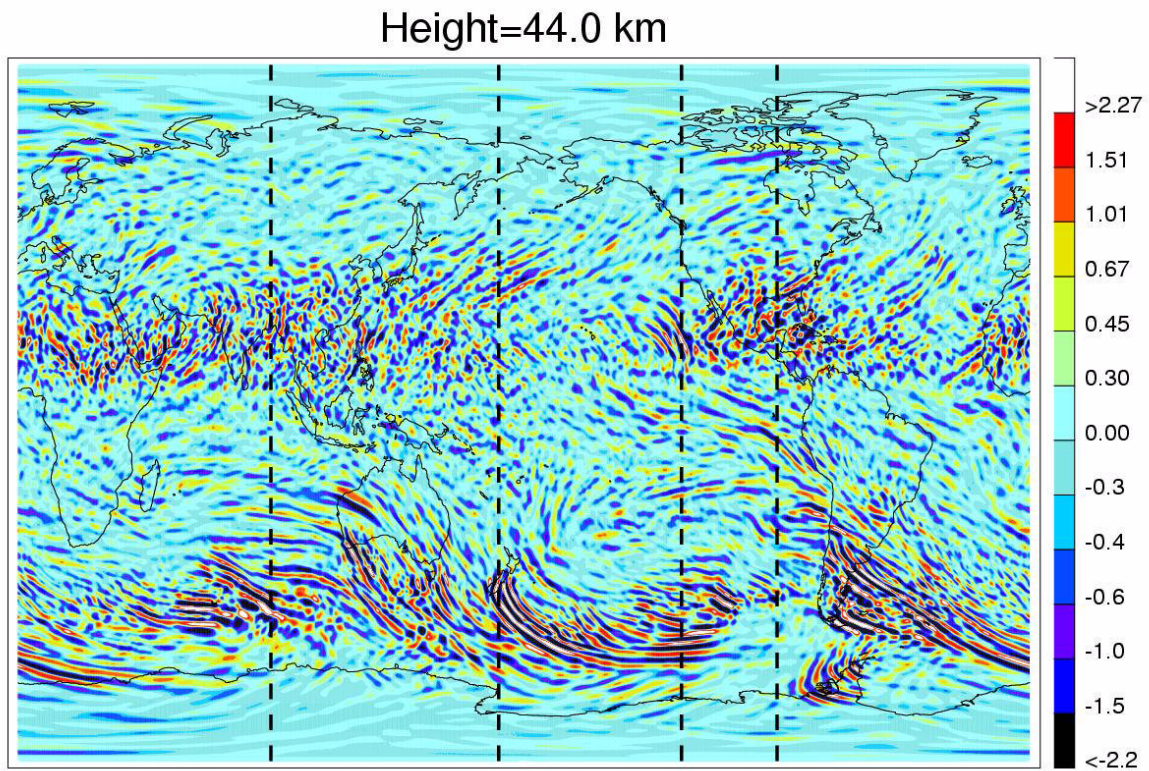


Figure 10. Temperature perturbation map from the ECMWF T_{L799L91} analysis fields at 44 km pressure altitude at 0000 UTC on 20 August 2006. Color scale has units of Kelvin. A 2D horizontal high-pass filter was applied to extract small-scale structure, which corresponds to a long wavelength cutoff of ~300 km at low and middle latitudes. Dotted lines indicate the cross sections to be shown in Fig.11 at 82°E, 171°E, 236°E and 297°E longitudes.

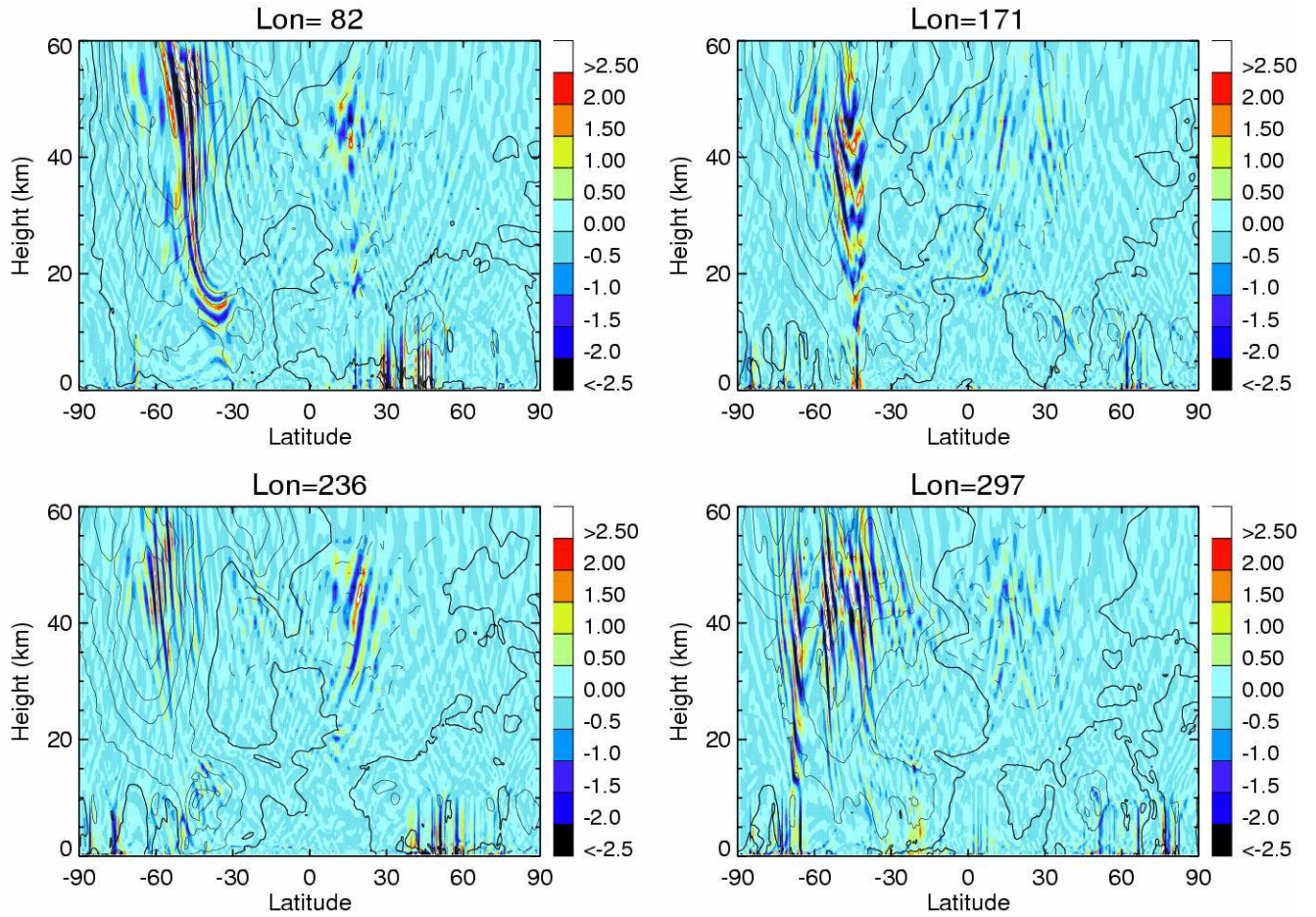


Figure 11. Cross-sections of temperature perturbations (in Kelvin, see color bars) as a function of latitude and pressure altitude from the ECMWF T_{L799L91} analysis fields on 20 August 2006 at 0000 UTC at the selected longitudes shown in the title (in degrees east) and highlighted in Fig. 10. Contours lines are the background zonal winds from the ECMWF IFS analysis at that longitude and have increments of 10 m/s with dashed (solid) lines denoting westward (eastward) values.

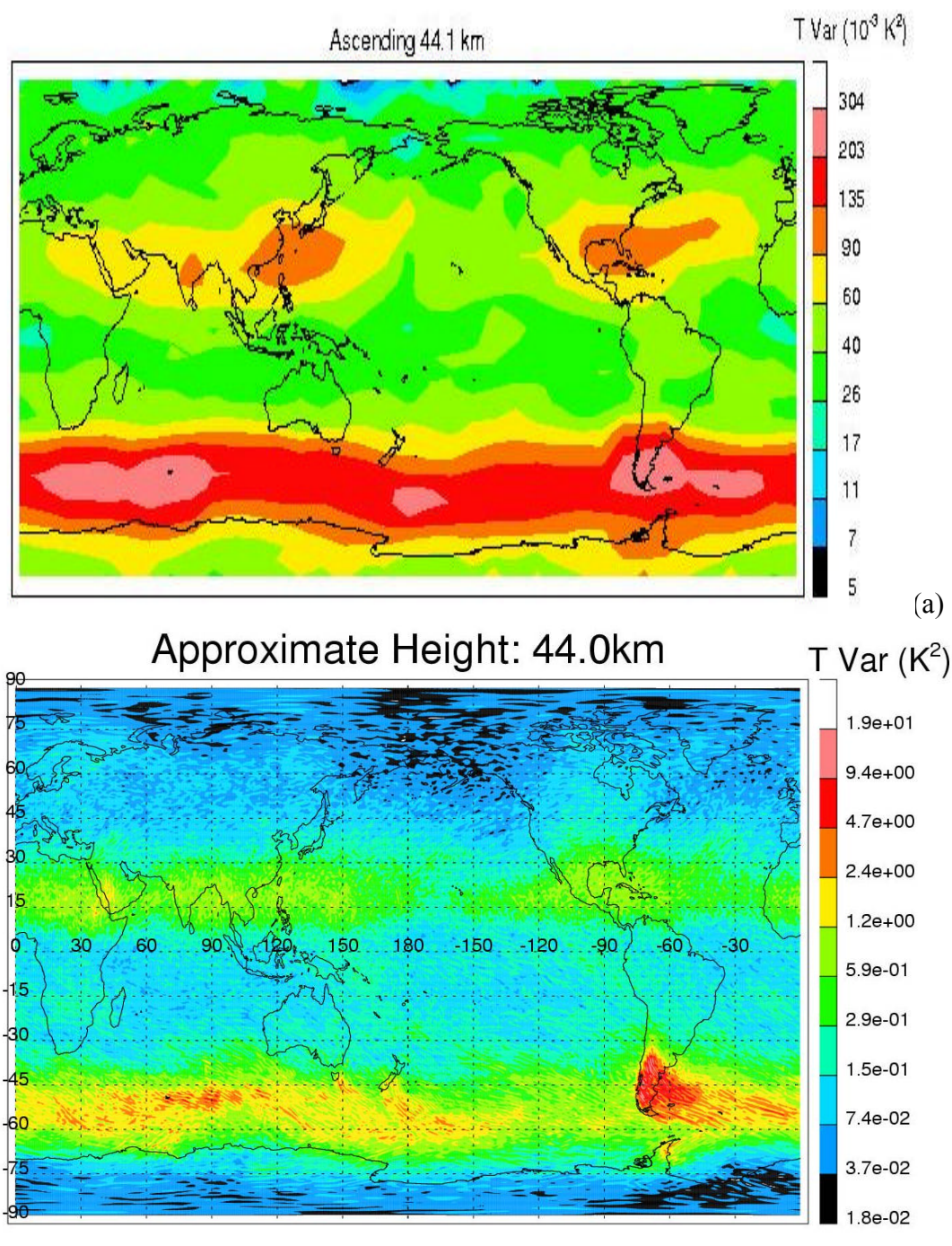


Figure 12. Map of monthly-mean GW temperature variance at ~44 km pressure altitude from (a) Aura MLS GW variance from Channels 11/15, and (b) ECMWF IFS T_{L799L91} analyses for every day of August 2006. As in Figs. 10-11, temperature perturbations in the ECMWF IFS analyses were truncated to exclude horizontal wavelengths > ~300 km before the variance was computed, but no vertical filter was applied.

Table

Table 1. Aura MLS 118 GHz radiance noise in the normal operation

MLS Channels	Saturation Height (km)	Instrument $\sigma_e^2(n)_a$ (K ²)	Min. Detectable GW Variance ($\times 10^{-3}$ K ²)			
			Maps ^b		Zonal Mean ^c	
			Monthly	5-day	Monthly	Daily
1 (25)	21.7	0.061	2.3	5.6	0.38	2.3
2 (24)	23.0	0.065	2.4	5.9	0.4	2.4
3 (23)	24.3	0.065	2.4	5.9	0.4	2.4
4 (22)	25.6	0.095	3.5	8.6	0.59	3.5
5 (21)	27.3	0.094	3.5	8.5	0.58	3.5
6 (20)	29.1	0.098	3.7	8.9	0.61	3.7
7 (19)	31.9	0.12	4.6	11	0.77	4.6
8 (18)	34.3	0.19	7.0	17	1.2	7.0
9 (17)	37.0	0.24	8.9	22	1.5	8.9
10 (16)	40.1	0.36	13	33	2.2	13
11 (15)	44.1	0.46	17	42	2.9	17
12 (14)	50.8	0.69	26	63	4.3	26

- a) This noise variance is approximately one half of single-channel noise variance as a result of combining the symmetric channel pairs.
- b) A grid box of 5°×10° latitude-longitude is used in this averaging.
- c) These zonal means have a 5° latitude bin.